Nano Research

Open Access

Research Article

Simultaneously supplementing Wtp53 and degrading Mutp53 using a virus-mimicking mRNA delivery system to restore P53's autonomous anti-cancer function

Yan Liang[1], Chenlu Xu[1], Jingge Zhang[1], Shuguang Li[1], Menghao Yin[1], Yinchao Li[1] ✉, Hua Gao[2] ✉, and Kaixiang Zhang[1,3] ✉

[1] *School of Pharmaceutical Sciences, Tianjian Laboratory of Advanced Biomedical Sciences, Zhengzhou University, Zhengzhou 450001, China*
[2] *Department of pathogen biology, School of Basic Medical Sciences, Zhengzhou University, Zhengzhou 450001, China*
[3] *Beijing Life Science Academy, Beijing 102209, China*

Cite this article: *Nano Research*, **2025**, *18*, 94907529. https://doi.org/10.26599/NR.2025.94907529

ABSTRACT: Restoring P53's autonomous anti-cancer function through *P53* mRNA delivery is a promising anti-tumor strategy. Yet, in tumors harboring mutant *P53*, the existing mutant *P53* (Mutp53) would interferes with the anti-tumor function of Wtp53 through dominant-negative effect. Herein, we designed Vir-Z@R, a *P53*-repair nanosystem based on a virus-mimicking nanostructure to deliver *P53* mRNA and Zn(II) into tumor cells. By supplementing Wtp53 through *P53* mRNA delivery and promoting the degradation of mutant P53 via a zinc ion-mediated proteasomal pathway, Vir-Z@R restores the autonomous tumor-suppressive function of P53 and induce tumor cell death through multiple mechanisms (interfering with energy metabolism and inducing apoptosis), leading to delayed tumor growth and prolonged survival in mice with Mutp53. This study provides a strategy for treatment of P53-mutant tumor.

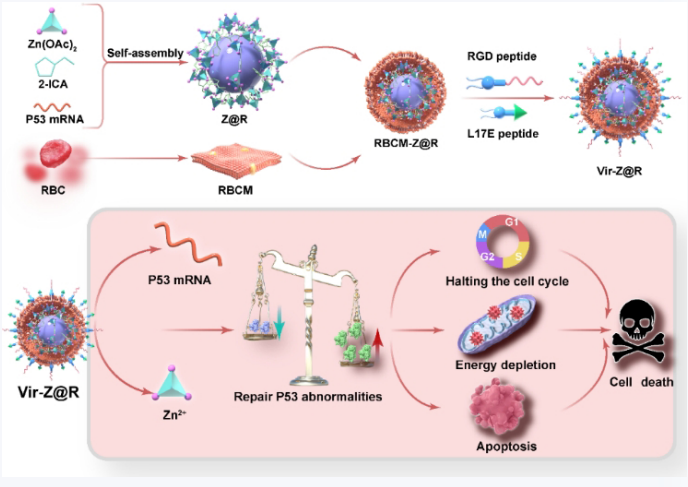

KEYWORDS: P53 function restore, mRNA delivery, antitumor therapy, virus-mimicking nanostructure, Zn(II)

1 Introduction

The tumor suppressor P53 is a transcription factor that is activated in response to DNA damage to trigger different cellular outcomes, such as cell cycle arrest, senescence and apoptosis, exerting autonomous tumor-suppressing functions [1–3]. However, absence of P53 expression or expression of mutant P53 (Mutp53) are common in human cancers, and are thought to be drivers of a variety of tumors [4]. And so, P53 restoration has long been considered an attractive anticancer strategy [5]. However, for decades, these attempts have largely been unsuccessful, with few *P53*-targeting drugs advancing to late-stage clinical development, and none receiving approval from the U.S. Food and Drug Administration (FDA) or European Medicines Agency (EMA) to date [6]. This may be due to the fact that, as a nuclear transcription factor, P53 lacks the typical characteristics of a druggable target, and the transfection of *P53* DNA carries the risk of genomic integration. As an emerging therapeutic approach, messenger RNA delivery may give a boost to P53 restoration-based cancer therapy [7].

At present, the delivery of *P53* mRNA into P53-deficient tumor cells using lipid nanoparticles has demonstrated efficacy in enhancing wild-type P53 protein (Wtp53) levels and reinstating its tumor-suppressive activity [8,9]. Yet, in tumors harboring mutant P53, the existing Mutp53 not only affects the tumor suppressor function of Wtp53, but also improves tumor proliferation and metastasis through gain-of-function (GOF) mechanisms, and exerts a dominant-negative effect by inhibiting the function of Wtp53 [10–13]. Therefore, it is necessary to degrade Mutp53 while supplementing Wtp53.

Received: November 5, 2024; **Revised:** April 8, 2025
Accepted: April 30, 2025

✉Address correspondence to Yinchao Li, lych@zzu.edu.cn; Hua Gao, gaohua212@zzu.edu.cn; Kaixiang Zhang, zhangkx@zzu.edu.cn

It's found that high intracellular Zn(II) levels lead to generation of endogenous reactive oxygen species (ROS), which can induce the specific degradation of Mutp53 via the ubiquitin-proteasome system (UPS) pathway [14–17]. This may be due to the fact that Mutp53 often exhibits misfolded conformations with exposed cysteine residues that are sensitive to Zn(II)-mediated oxidative aggregation. However, for Wtp53, Zn(II) could bind to the DNA-binding domain, maintaining the structural integrity of Wtp53 and facilitating its transcriptional activation function [18, 19]. Thus, Zn(II) carriers capable of delivering *P53* mRNA may offer a new approach for simultaneously supplementing Wtp53 and degrading Mutp53 to restore P53's autonomous anti-cancer function.

Herein, a virus-mimicking nanostructure (Vir-Z@R) was designed for the treatment of P53-mutant tumors by co-delivery of *P53* mRNA and Zn(II) (Fig. 1). This nano-system encapsulates *P53* mRNA with Zeolitic imidazolate framework-90 (ZIF-90) nanoparticles, covered by red blood cell membranes (RBCMs), and further modified with arginine-glycine-aspartic acid peptide (RGD peptide, tumor-targeting peptide) and L17E peptide (lysosome escape peptide) to form the virus-mimicking nanoparticle Vir-Z@R. Vir-Z@R mimics the viral structure and promotes the transfection of *P53* mRNA: (1) ZIF-90 nanoparticles encapsulate *P53* mRNA (Z@R) mimic viral nucleocapsid structures, protecting nucleic acids from degradation. (2) The red blood cell membrane mimics the viral envelope, effectively avoiding immune clearance and prolonging circulation in the bloodstream. (3) The RGD peptide and L17E peptide mimic the glycoprotein spikes on the virus surface, enabling Vir-Z@R to specifically target tumor cells via $\alpha v\beta 3$ integrin receptor-mediated endocytosis and achieve efficient lysosome escape. (4) Z@R can respond to adenosine triphosphate (ATP) to decompose within the tumor cytoplasm, releasing *P53* mRNA and Zn(II) to achieve supplementation of Wtp53 and degradation of Mutp53, thereby activating apoptotic pathways, halting the cell cycle, and suppressing tumor energy metabolism, offering a promising way for treating *P53* mutant tumors.

2 Results and discussion

2.1 Synthesis and characterization of Vir-Z@R

To prepare virus-mimicking nanoparticles for effective restoration of the autonomous tumor suppressor function of P53 in tumor cells, we firstly synthesized nano-scale ZIF-90 through the self-assembly process of 2-ICA and $Zn(CH_3COOH)_2{\cdot}2H_2O$. ZIF-90 possesses the capability to release biomolecules and zinc ions in response to ATP decomposition. This characteristic makes it an ideal carrier for delivering *P53* mRNA into tumor cells carrying P53 mutations. Transmission electron microscopy (TEM) confirmed the homogeneous dispersion of ZIF-90, displaying its characteristic rhombic dodecahedral structure (Fig. 2(a)) [20]. Subsequently, the Z@R, mimicking the nucleocapsid structure of viruses, was synthesized by incorporating *P53* mRNA during the self-assembly of 2-ICA and $Zn(CH_3COOH)_2{\cdot}2H_2O$. To optimize the loading of *P53* mRNA, we investigated the impact of varying amounts of *P53* mRNA on the particle size and RNA encapsulation efficiency of Z@R. Within a 500 μL Z@R preparation system, employing 10 μg of *P53* mRNA resulted in a notably higher RNA encapsulation efficiency (72.83%) with a minimal particle size of approximately 167.5 ± 10.3 nm (Fig. S1(a) in the Electronic Supplementary Material (ESM)). Consequently, 10 μg of *P53* mRNA was chosen for Z@R preparation in each 500 μL Z@R preparation system.

TEM images revealed that the resulting Z@R nanoparticles were uniformly dispersed and retained the rhombic dodecahedral structure (Fig. 2(a)), indicating that the loading of P53 mRNA did not alter the morphology of ZIF-90. Additionally, dynamic light scattering (DLS) results exhibited that the size of Z@R is 167.1 ± 8.0 nm, with a potential of 14.68 ± 0.97 mV, both smaller than those of ZIF-90 (Figs. 2(b) and 2(c)). This reduction may be attributed to the faster nucleation of Z@R due to the strong coordination interaction between Zn(II) and *P53* mRNA [21]. Furthermore, high-angle annular dark-field scanning TEM (HAADF-STEM) images demonstrated the presence of characteristic zinc elements from ZIF-90 and phosphorus elements from *P53* mRNA within Z@R (Fig. 2(d)), confirming the effective loading of *P53* mRNA into Z@R. X-ray diffraction (XRD) was carried out to investigate whether RNA molecules influenced the ZIF-90 crystals within Z@R (Fig. 2(e)). The findings revealed no significant shifts in peak positions compared to ZIF-90, suggesting that the process of loading *P53* mRNA had minimal impact on the lattice structure of ZIF-90, which is expected to retain the in response to ATP decomposition properties of ZIF-90 [22–24]. Subsequently, the surface chemistry of Z@R was assessed using X-ray photoelectron spectroscopy (XPS) analysis. The results showed the presence of Zn(II) on the surface of Z@R, indicating that *P53* mRNA was encapsulated within the interior of ZIF-90 rather than on the surface (Fig. 2(f)). This virus-mimicking nucleocapsid structure contributes to stable storage of mRNA. The capillary electrophoresis analysis results indicating that Z@R could stably store mRNA at 4 °C for up to 9 days (Figs. 2(g) and 2(h)), further confirming this conclusion.

Next, RBCM was coated on Z@R (yielding RBCM-Z@R) to mimic the viral envelope used to protect the nanoparticles from the immune system. The DLS results showed that the particle size of RBCM-Z@R increases to 208.9 ± 8.7 nm, and the potential changes to −22.53 ± 0.21 mV, confirming the successful camouflage with RBCM (Figs. 2(b) and 2(c)). To assess the content of *P53* mRNA and RBCM in RBCM-Z@R, we investigated the thermal stability of ZIF-90, Z@R, and RBCM-Z@R through thermogravimetric analysis (TGA). The results indicated that a payload of *P53* mRNA at 7.1 wt.% and a modification quantity of RBCM at 1.8 wt.% (Fig. 2(i)), suggesting that ZIF-90 is a promising nano-carrier for transporting mRNA and achieving surface functionalization.

Finally, 1,2-distearoyl-sn-glycero-3-phosphoethanolamine-polyethylene glycol-RGD (DSPE-PEG-RGD) peptide (facilitating tumor cell recognition) and DSPE-PEG-L17E (facilitating lysosomal escape) peptide (Table S2 in the ESM) simulating the spike glycoprotein were modified on RBCM via a lipid-insertion approach to complete the structural mimicry of virus (yielding Vir-Z@R). The loading amount of the two peptides in Vir-Z@R was investigated by the fluorescence intensity of RGD peptide (fluorescein isothiocyanate (FITC) labeled) and L17E peptide (Cy5 labeled). Results of fluorescence intensity showed that the modification rate of RGD peptide and L17E peptide was about 26.5% and 36.7%, respectively (Fig. S1(b) in the ESM). TEM images showed that the RBCM vesicles had a hollow structure with an average size of 100 nm. Vir-Z@R had a uniform and spherical structure with a unilamellar membrane coating (Fig. 2(a)). The DLS results indicated that the size of Vir-Z@R is 213.8 ± 3.6 nm, with a potential of −23.03 ± 0.66 mV (Figs. 2(b) and 2(c)), suggesting that

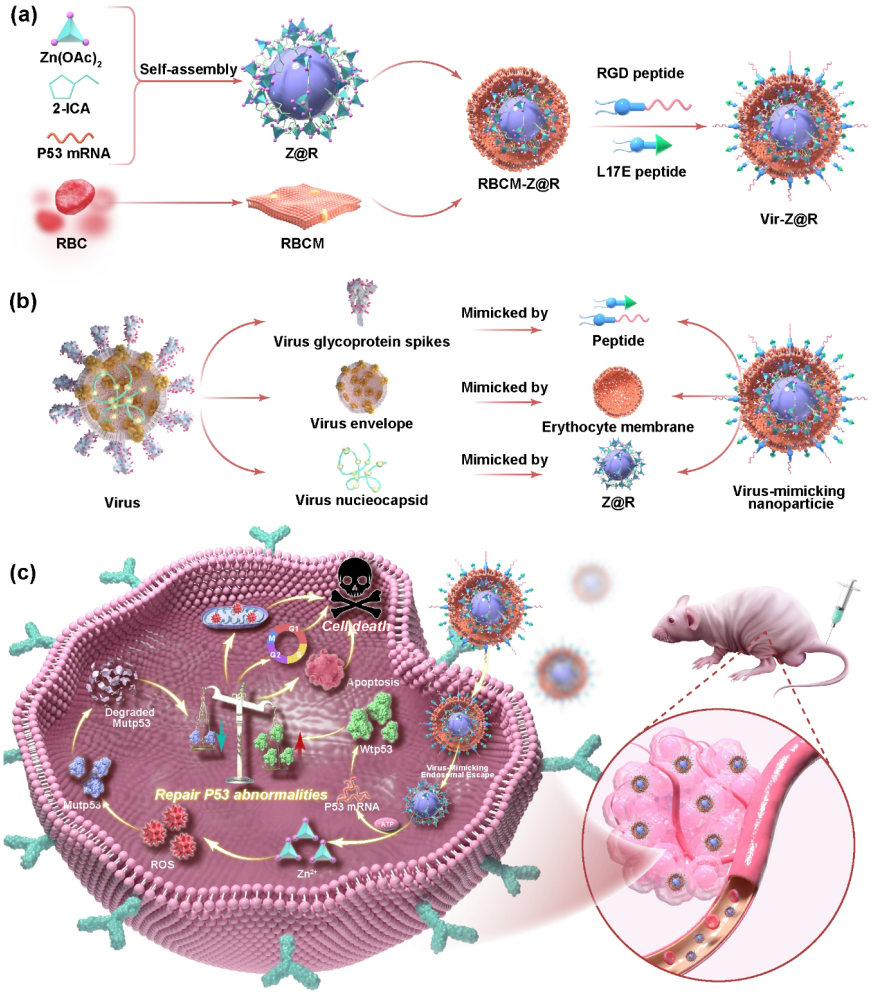

Figure 1 Schematic diagram of Vir-Z@R simultaneously complementing Wtp53 and degrading Mutp53 to synergistically enhance tumor therapy. (a) Schematic representation of Vir-Z@R synthesis. (b) Schematic representation of Vir-Z@R mimicking viral structure. (c) Schematic representation of Vir-Z@R *in vivo* mechanism of action.

the peptide modification does not have a significant effect on the particle size and potential of the nanoparticles.

Surface membrane proteins of red blood cells (RBCs), such as CD47, enable nanoparticles to evade immune clearance, thereby prolonging their circulation time *in vivo* [25]. The protein composition of the RBCM and Vir-Z@R was analyzed using sodium dodecyl sulfate-polyacrylamide gel electrophoresis (SDS-PAGE). The result indicated that Vir-Z@R had a protein composition similar to that of RBCs and RBCMs (Fig. 2(j)). Western blot (WB) analysis further demonstrated that RBCMs and Vir-Z@R were devoid of hemoglobin (Hb), while retaining several key membrane proteins, including CD41, CD47 and CD235*α* (Fig. 2(k)), which provided the basis for long circulation *in vivo* of Vir-Z@R. Next, using DLS and the RiboGreen RNA assay kit, the changes in particle size, polydispersity index (PDI), and encapsulation efficiency of Vir-Z@R and Z@R dispersed in phosphate-buffered saline (PBS) and 10% fetal bovine serum (FBS) over the course of one week were compared (Fig. S1(d) in the ESM). The results indicated that Z@R struggles to maintain stability in both PBS and 10% FBS. However, the peptide modified RBCM enhanced the stability of Vir-Z@R in both PBS and 10% FBS. In addition, the hemolysis test results also confirmed the good blood compatibility of Vir-Z@R (Fig. S1(c) in the ESM). The above results suggested that Vir-Z@R possesses excellent stability and suitability for *in vivo* application.

The L17E peptide-mediated disruption of the endosomal membrane can facilitate the escape of Z@R from the lysosome into the cytoplasm. Due to the stronger coordination of ATP with Zn(II) than imidazole, Z@R is expected to respond to the high concentration of ATP in the cytoplasm of tumor cells, releasing Zn(II) and *P53* mRNA (Fig. S1(e) in the ESM). The TEM and DLS results indicated that Z@R underwent partial disintegration upon the addition of 2 mM ATP, resulting in a decrease in particle size to 123.5 ± 10 nm. Furthermore, complete collapse of Z@R occurred within 10 min following treatment with 5 mM ATP, leading to a further reduction in particle size to 36.7 ± 10.0 nm.

Next, we quantitatively analyzed Zn(II) and *P53* mRNA released from Z@R. As shown in Fig. 2(l), the release of *P53* mRNA was negligible in the absence of ATP. However, the release increased with rising ATP concentrations, culminating in a cumulative release rate reached 86% after treatment with 5 mM ATP for 1 h. Additionally, the efficient release of Zn(II) from Z@R was confirmed by inductively coupled plasma mass spectrometry (ICP-MS) (Fig. 2(m)). This laying the foundation for subsequent intracellular biological functions of Zn(II) and *P53* mRNA.

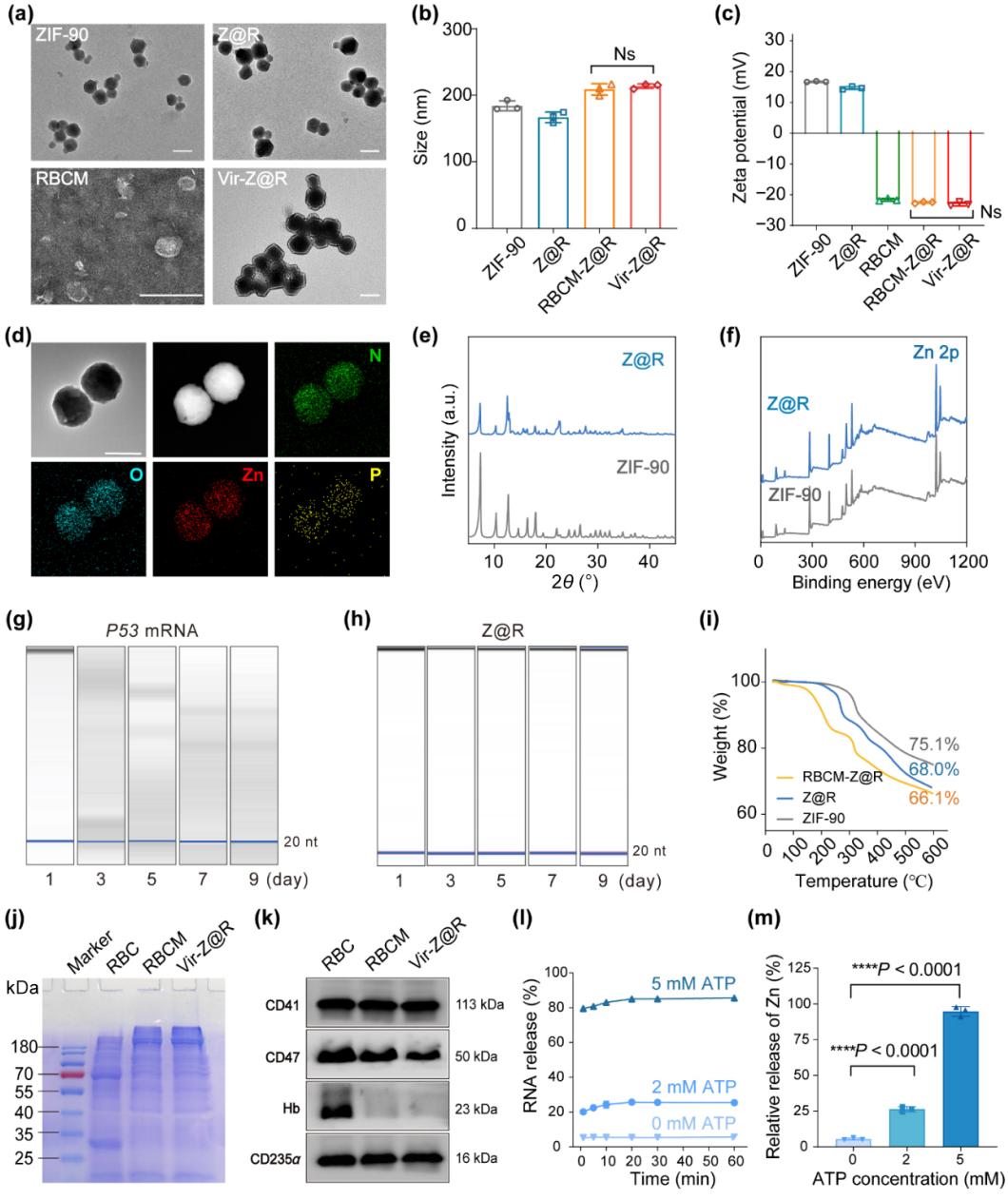

Figure 2 Preparation and construction of Vir-Z@R. (a) TEM images of ZIF-90, Z@R, RBCM and Vir-Z@R. Scale bars: 200 nm. (b) The size of ZIF-90, Z@R, RBCM-Z@R and Vir-Z@R (n = 3). (c) Zeta potentials of ZIF-90, Z@R, RBCM, RBCM- Z@R and Vir-Z@R (n = 3). (d) TEM mapping analysis of Z@R. Scale bar: 200 nm. (e) XRD analysis of ZIF-90 and Z@R. (f) XPS analysis of ZIF-90 and Z@R. (g) Capillary electrophoresis analysis of *P53* mRNA stability under 4 ℃ conditions. (h) Capillary electrophoresis analysis of *P53* mRNA stability in Z@R under 4 ℃ conditions. (i) TGA analysis of ZIF-90, Z@R and RBCM-Z@R. (j) Protein composition of RBCs (red blood cells), RBCMs and Vir-Z@R analyzed by SDS-PAGE. (k) Western blot analysis of CD41, CD47, Hb and CD235α in RBCs, RBCMs and Vir-Z@R. (l) RNA release profiles of 0, 2 and 5 mM ATP treated Z@R determined by fluorescence spectrophotometry (n = 3). (m) Zn(II) release profiles of 0, 2 and 5 mM ATP treated Z@R measured by ICP-MS (n = 3). Data in (b), (c), (l) and (m) are represented as mean ± standard deviation (SD). Statistical differences between the two groups were determined using unpaired two-tailed Student's t-test (*P < 0.05, **P < 0.01, ***P < 0.001 and ****P < 0.0001; Ns: no significance).

2.2 Functional characterization of Vir-Z@R

Rapid clearance of natural viruses by macrophages significantly diminishes their therapeutic efficacy. Initially, we examined whether RBCM modification could effectively inhibit the phagocytosis of Vir-Z@R by macrophages. L17E-RBCM-Z@R was synthesized as control [26]. To track the nanoparticles inside the cells, *P53* mRNA was labeled with Cy5. As shown in the flow cytometry analysis results, compared with Z@R, the uptake of Vir-Z@R and L17E-RBCM-Z@R by RAW 264.7 cells were significantly reduced (Fig. 3(a)), which indicated that RBCM modification can effectively reduce the phagocytosis of macrophages. Then, CLSM images and flow cytometry analysis demonstrated that, compared with Z@R and L17E-RBCM-Z@R, Vir-Z@R was internalized more efficiently into BxPC3 pancreatic carcinoma cells harboring Y220C mutation (Fig. 3(a) and Fig. S2 in the ESM). The enhanced cellular uptake was primarily dependent on the RGD peptide, which facilitated the uptake of Vir-Z@R by specifically binding to the $\alpha v\beta 3$ integrin on BxPC3 cells. Meanwhile, CLSM imaging also showed that the uptake of Vir-Z@R by BxPC3 cells was related to time, the uptake

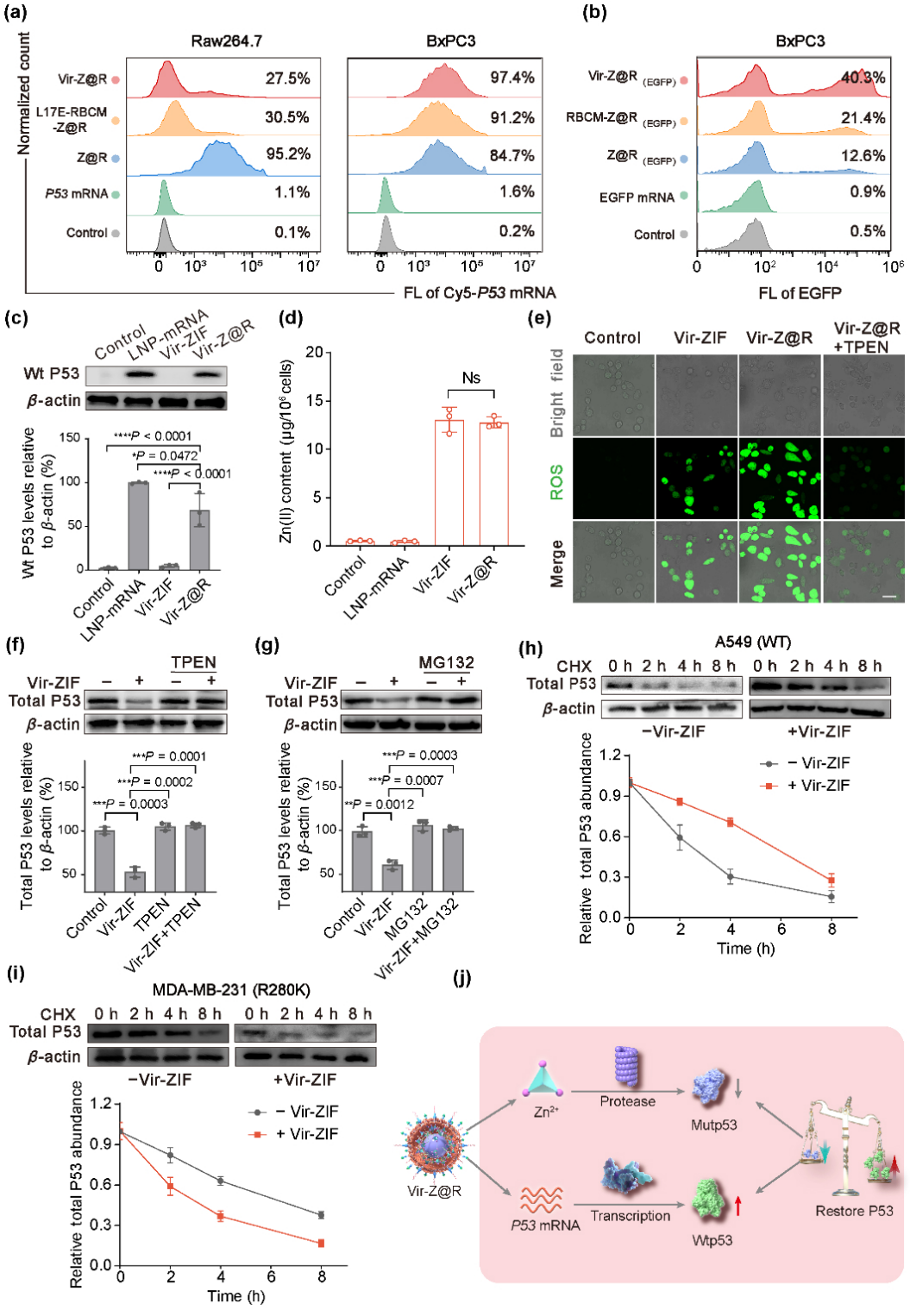

Figure 3 Functional characterization of Vir-Z@R. (a) Flow cytometry analysis of Raw264.7 and BxPC3 cells co-incubated with *P53* mRNA, Z@R, L17E-RBCM-Z@R, and Vir-Z@R treatment for 4 h (left and right). RNA was labeled with Cy5. (b) BxPC3 cells co-incubated with EGFP mRNA, Z@R(EGFP), RBCM-Z@R(EGFP), and Vir-Z@R(EGFP), and transfection efficiency was measured after 24 h. (c) Following 8-h treatment with LNP-mRNA, Vir-ZIF, and Vir-Z@R, Western blot analysis assessed Wt P53 levels in BxPC3 cells, followed by quantification. (d) Quantification of intracellular Zn(II) elevated by non-treated Control, LNP-mRNA, Vir-ZIF, and Vir-Z@R using ICP-MS (n = 3). (e) Fluorescence images of intracellular free ROS production (green) after various treatments (Control, Vir-ZIF, Vir-Z@R and Vir-Z@R+TPEN co-treatment) were measured by CLSM. Scale bar: 20 μm. Western blot analysis of total P53 in BxPC3 cells after the indicated treatment for 8 h. Dosing: (f) TPEN, 10 μM; (g) MG132, 10 μM. Western blot of (h) A549 and (i) MDA-MB-231 cells treated with Vir-ZIF NPs or not for 8 h and then treated with 100 μg/mL cycloheximide (CHX) at the indicated time points, n = 3 biologically independent samples, relative P53/actin ratios are shown. (j) Schematic representation of Vir-Z@R's P53 restore function in cells. Data in (c), (d), (f), (g), (h) and (i) are presented as mean ± SD. Statistical differences between the two groups were determined using unpaired two-tailed Student's t-test (*P < 0.05, **P < 0.01, ***P < 0.001, and ****P < 0.0001; Ns: no significance).

increased gradually with the prolongation of culture time (Fig. S3 in the ESM).

To visualize endosomal escape, *P53* mRNA were labeled with Cy5 and the endosomes were stained with LysoTracker Green. As displayed Fig. S4 in the ESM, *P53* mRNA (red fluorescence) and endosomes (green fluorescence) were well colocalized at 1 h, indicating the endocytosis of RGD-RBCM-Z@R and Vir-Z@R. For Vir-Z@R-treated cells, red fluorescence signals were observed outside the endosomes at 2 h, and moreover permeated into the cytosol at 4 h. However, the intracellular RGD-RBCM-Z@R signals remained colocalized with the endosomes even at 4 h. These results demonstrated that Vir-Z@R achieve endosomal escape through L17E peptide-mediated membrane fusion following endocytosis [27]. We then employed CLSM and flow cytometry to investigate the transfection efficiency of Vir-Z@R(EGFP) in BxPC3 cells (Fig. 3(b) and Fig. S5 in the ESM). RBCM-Z@R(EGFP) was used as a control to explore the effect of peptide modification on transfection efficiency. Following transfection, Z@R(EGFP) achieved 12.6% enhanced green fluorescent protein (EGFP) positive cells higher than 0.9% in the EGFP mRNA group, which may be due to the promotion of EGFP mRNA uptake by Z@R. As expected, the Vir-Z@R(EGFP) group exhibited significantly higher fractions of EGFP-positive cells (40.3%) than the RBCM-Z@R(EGFP) groups (21.4%), which indicated that this virus-mimicking nanoparticles can achieve efficient mRNA delivery by highly simulating the structure and mechanism of viruses *in vivo*.

To assess the impact of Vir-Z@R on *P53* mutant tumor cell lines, we next examined P53 stability in BxPC3 pancreatic carcinoma model harboring a *P53* conformational mutation (Y220C). Lipid nanoparticles (LNPs) have emerged as highly successful mRNA delivery vehicles, already in clinical use [28]. Therefore, we prepared LNP-mRNA as a zinc ion-free control group. Simultaneously, Vir-ZIF was employed as a control lacking *P53* mRNA. Results indicated that treatment with Vir-Z@R and LNP-mRNA significantly elevated levels of Wtp53 proteins within BxPC3 cells, whereas the Vir-ZIF group exhibited no impact on Wtp53 protein levels, suggesting that Vir-Z@R potentially upgrades Wtp53 protein via releasing Zn(II) and *P53* mRNA (Fig. 3(c)). Notably, ICP-MS confirmed that Vir-ZIF and Vir-Z@R treated cells successfully induced an increase in intracellular Zn(II) concentration with up to 12.8 μg/10^6 cells (Fig. 3(d)). Vir-ZIF effectively stimulated the production of ROS by releasing Zn(II), and Vir-Z@R produced more reactive oxygen species than Vir-ZIF, which may be due to the further amplification of oxidative stress by the expression of P53 protein (Fig. 3(e) and Fig. S6 in the ESM).

In addition, to validate the effect of Zn(II) on Mutp53 protein, cells treated with Vir-ZIF were subjected to a cell-permeable Zn(II) chelator (TPEN). Results showed complete abrogation of Vir-ZIF-induced Mutp53 protein degradation upon TPEN treatment (Fig. 3(f)), demonstrating the necessity of intracellular Zn(II) elevation for Vir-ZIF-mediated Mutp53 degradation. Inhibition of ROS by antioxidant N-acetylcysteine (NAC) and proteasome inhibition by MG132 noticeably hindered Vir-ZIF-induced Mutp53 protein degradation (Fig. 3(g) and Fig. S7 in the ESM), confirming that Vir-ZIF-mediated Mutp53 protein degradation occurs via ROS-mediated the ubiquitination-dependent proteasome pathway [29, 30]. Thus, intracellular ROS elevation is crucial toward Mutp53 proteasomal degradation induced by Vir-ZIF. To further determine whether such decreased Mutp53 level was from a reduced transcription, we conducted quantitative real-time polymerase chain reaction (qRT-PCR) analysis to the cells with different treatments. Interestingly, no difference in *P53* mRNA expression was seen with Vir-ZIF from that of control group (Fig. S8 and Table S1 in the ESM), indicating that neither Zn(II) nor ROS released from Vir-ZIF altered the transcription of Mutp53 and the corresponding Mutp53 reduction most likely occurred through the post-translational degradation.

To rule out the cell-type specific effect of Zn(II) on P53 stability, we assessed its impact on A549 (human lung cancer with wild-type P53 expression) and MDA-MB-231 (breast cancer cells expressing the P53-R280K contact mutant). As depicted in the Fig. 3(h), the cycloheximide (CHX) chase assay results showed that Vir-ZIF significantly increased the half-life of Wtp53 within 8 h in A549 cell lines, confirming the stabilizing effect of Zn(II) on Wtp53 protein [31]. In addition, Vir-ZIF significantly promoted P53 protein degradation in MDA-MB-231 cells (Fig. 3(i)), indicating that Vir-ZIF did not have a clear preference for the category of the mutants being eliminated. Consistent with results obtained in the BxPC3 cell line, that treatment with Vir-Z@R significantly elevated levels of total P53 proteins within MDA-MB-231 cells (Fig. S9 in the ESM).

To further analyze whether Vir-ZIF-mediated degradation of Mutp53 occurs through the ROS-mediated ubiquitination-dependent proteasomal pathway, we validated the ubiquitination of cellular proteins in Vir-ZIF-treated cells via co-immunoprecipitation. The results demonstrated that Vir-ZIF enhanced the overall ubiquitination of cellular proteins, particularly K48-linked polyubiquitination, highlighting its effectiveness in promoting Mutp53 degradation. Furthermore, treatment with MG132 led to a further increase in Mutp53 ubiquitination, while the ubiquitination inhibitor PYR-41 abolished the Mutp53 degradation activity of Vir-ZIF (Fig. S10 in the ESM). These findings confirm that Vir-ZIF facilitates Mutp53 degradation via a ubiquitination-dependent proteasomal pathway. These observations suggested that Zn^{2+} can distinguish the conformation of Mutp53 and Wtp53, thereby enabling Vir-ZIF exhibits varying effects on mutated and wild-type P53 proteins, showing the potential of restore P53 protein (Fig. 3(j)).

2.3 Performance and cytotoxicity study of Vir-Z@R *in vitro*

Having demonstrated that Vir-Z@R can achieve regulation of P53 protein in tumor cells, maintaining stability of Wtp53 while degrading Mutp53. To analyze whether Vir-Z@R could restore the natural tumor-suppressing function by regulation P53 [32], the cell counting kit-8 (CCK-8) assay was firstly employed to determine the optimal dose concentration through the cell viability of BxPC3 cells treated with different concentrations of Vir-Z@R for 24 h, with Vir-ZIF devoid of *P53* mRNA serving as the control group for comparison. As shown in Fig. 4(a), after incubation with BxPC3 cell, different doses of Vir-Z@R and Vir-ZIF induced strong cytotoxicity in a dose-dependent manner. At a concentration of 50 μg/mL, the Vir-Z@R group exhibited greater cytotoxicity compared to the Vir-ZIF group, indicating that Vir-Z@R facilitated tumor cell death by delivering *P53* mRNA. Additionally, we assessed the effect of Vir-Z@R on the viability of Raw264.7 cells, DC2.4 cells, and spleen-derived T cells using the CCK-8 assay. As shown in the Fig. S11 in the ESM, Vir-Z@R at a concentration of 50 μg/mL exhibited no significant cytotoxicity toward these non-tumor cells. This may be attributed to the immune evasion

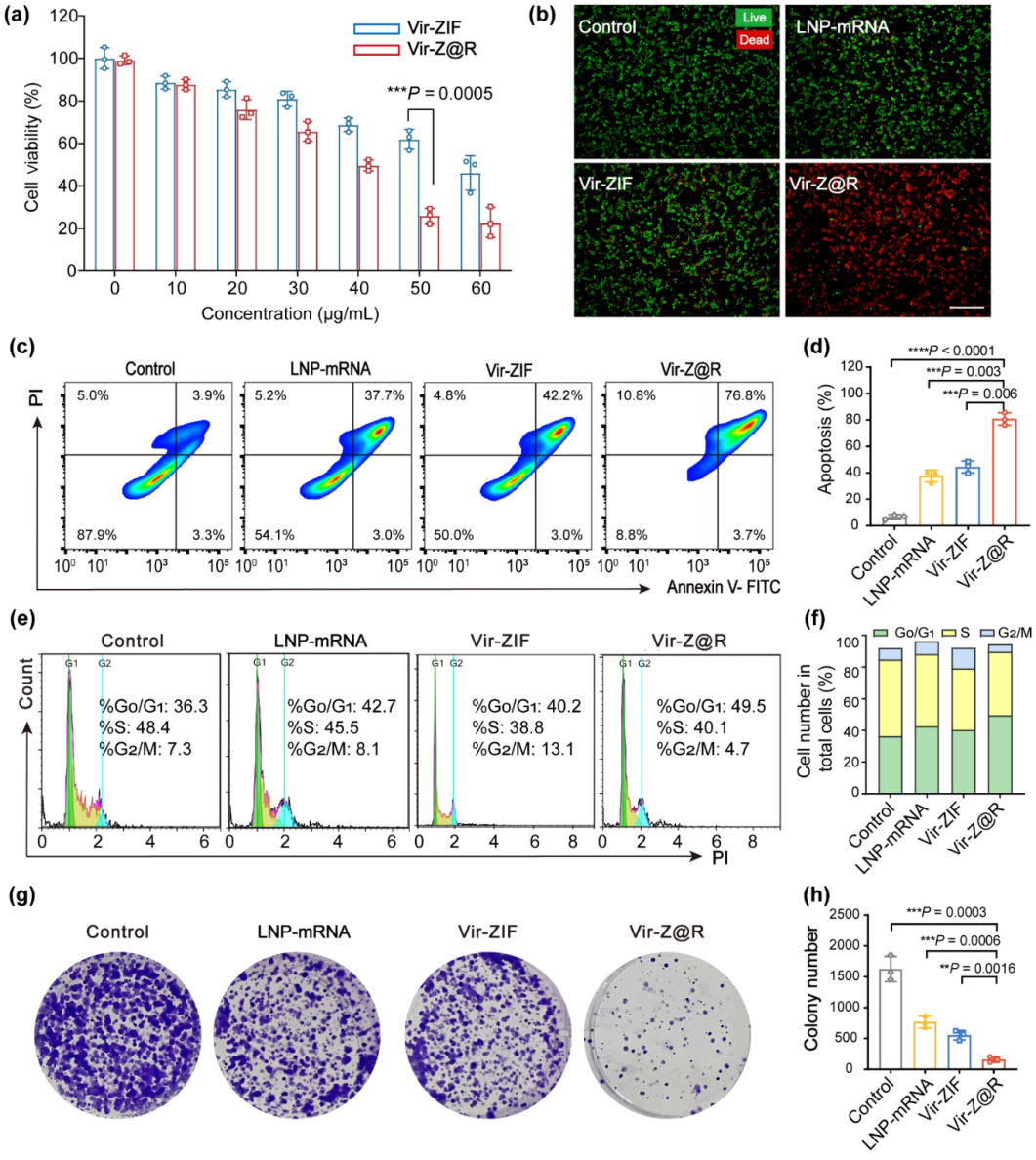

Figure 4 The *in vitro* anticancer activity and mechanism of action of Vir-Z@R nanoparticles. (a) Viability of BxPC3 cells treated with indicated concentrations of Vir-ZIF and Vir-Z@R (n = 3). (b) Fluorescence images of BxPC3 cells after treatment with Control, LNP-mRNA, Vir-ZIF, and Vir-Z@R. Live cells (green) were stained with calcein-AM and dead cells (red) with PI. (c) BxPC3 cells were stained with Annexin V-FITC/PI and evaluated by flow cytometry to assess apoptosis following the indicated treatments, with (d) corresponding quantified results presented. (e) Flow cytometry analysis and (f) the quantitative assessment of cell cycle progression in BxPC3 cells treated with indicated formulations. (g) Colony formation assays and (h) the quantified results of BxPC3 cells treated with indicated agents. Data in (a), (d), (f), and (h) are presented as mean ± SD. Statistical differences between the two groups were determined using unpaired two-tailed Student's t-test (*P < 0.05, **P < 0.01, ***P < 0.001, and ****P < 0.0001; Ns: no significance).

properties of the RBCM. Given these observations, and to ensure effective degradation of Mutp53 protein by Zn(II) while maximizing the effect of *P53* mRNA, we selected a concentration of 50 μg/mL for Vir-Z@R in subsequent cellular experiments.

As a transcription factor, the P53 protein exerts autonomous tumor-suppressive effects by regulating multiple pathways such as cell cycle progression, apoptosis, and maintaining genomic stability. Therefore, to validate the inhibitory effect of Vir-Z@R on BxPC3 cells, we performed a calcein acetoxymethyl ester/propidium iodide (calcein AM/PI) staining assay to visually observe live and dead cells using fluorescent signals. Compared to the other groups, the Vir-Z@R group exhibited a significant reduction in green fluorescence intensity, demonstrating its exceptional *in vitro* anticancer efficacy (Fig. 4(b)). To further confirm this, we conducted flow cytometry to analyze cellular apoptosis, with the findings presented in Fig. 4(c). The percentage of apoptotic and necrotic cells in the Vir-Z@R group was 80.4%, markedly higher than the 45.2% observed in the Vir-ZIF group and the 40.7% in the LNP-mRNA group (Fig. 4(d)). Additionally, the cell cycle phase distribution was studied upon treatment with Vir-Z@R in BxPC3 cells. Figures 4(e) and 4(f) showed that BxPC3 cells treated with Vir-Z@R had a larger G1 and G2 population (54.2%) compared with 43.6% in the control group, which indicated that Vir-Z@R induces cell cycle arrest at the G1 and G2 phases. Colony formation was also markedly inhibited in BxPC3 cells treated with Vir-Z@R versus control group (Figs. 4(g) and 4(h)). Similar results were observed in cell migration

experiment, suggesting that Vir-Z@R could effectively induce G1-phase and G2-phase cell cycle arrest to inhibit cell proliferation (Fig. S12 in the ESM). These results demonstrated that Vir-Z@R promotes the death of P53-mutant tumor cells by repairing P53 protein, which is a viable strategy for precise anti-tumor therapy.

2.4 Antitumor mechanism study of Vir-Z@R *in vitro*

To further investigate the mechanisms of cell death induced by Vir-Z@R, RNA sequencing was performed on BxPC3 cells treated with Vir-Z@R, using untreated BxPC3 cells as the control. The inter-sample correlation heat map revealed distinct differences between groups and consistency within groups. As anticipated, a high correlation (r^2 > 0.8) was observed within each treatment group, whereas no significant correlation was found between the control and Vir-Z@R-treated groups, indicating that the observed gene expression changes were specifically induced by Vir-Z@R (Fig. S13 in the ESM). Differential expression analysis identified 6354 differentially expressed genes (DEG) between the control and Vir-Z@R-treated samples. Volcano plots further demonstrated that, among the 6354 DEGs, 3388 genes were upregulated and 2966 were downregulated in Vir-Z@R-treated. In BxPC3 cells (Fig. 5(a)), Kyoto encyclopedia of genes and genomes (KEGG) analysis of DEGs revealed that Vir-Z@R was involved in many biological processes, the significantly enriched pathways include cell apoptosis, cell cycle, oxidative phosphorylation, and glycolysis, among others (Fig. 5(b)). Among these, cell apoptosis mainly affects the

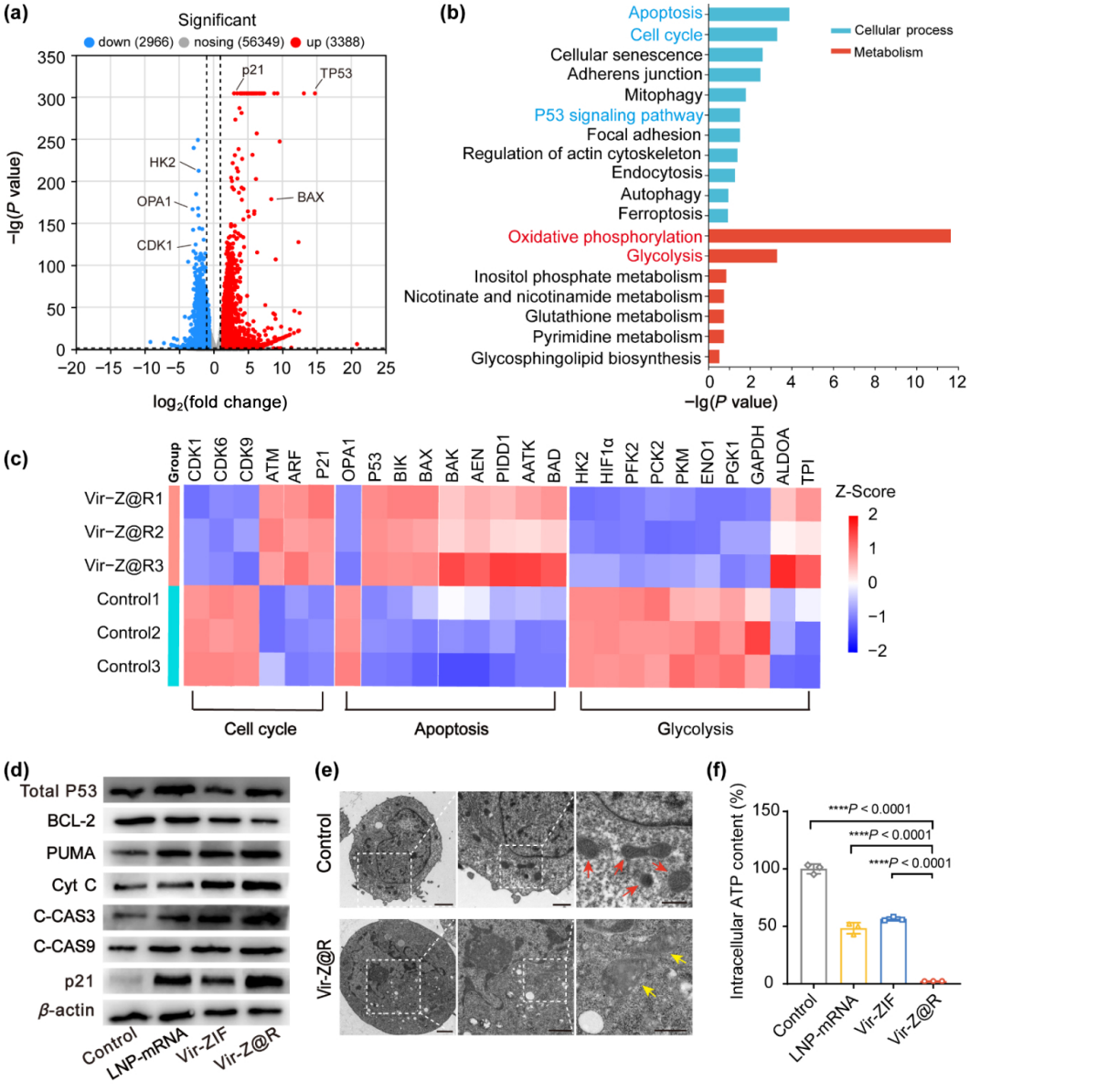

Figure 5 Transcriptome alterations caused by Vir-Z@R in BxPC3 cells. (a) Volcano plots of differentially expressed genes in Vir-Z@R treated BxPC3 cells in comparison with the control. Significantly regulated genes: adjusted *P* value ≤ 0.05 and a |log FC| ≥ 1. (b) KEGG pathway analysis, (c) gene heatmap in BxPC3 cells treated with Vir-Z@R compared to control. (d) Western blot analysis of total P53, BCL-2, PUMA, Cyt C, C-CAS3, C-CAS9 and p21 in BxPC3 cells after indicated treatments. *β*-actin was used as the loading control. (e) Representative bio-TEM images of BxPC3 cells treated with control or Vir-Z@R. Red arrows indicated normal mitochondria, and yellow arrows indicated swelling mitochondria. Scale bars: 2 μm (left images), 1 μm (middle images), and 500 nm (right images). (f) The ATP in BxPC3 cells after treatment with Control, LNP-mRNA, Vir-ZIF, and Vir-Z@R. Data in (f) are presented as mean ± SD. Statistical differences between the two groups were determined using unpaired two-tailed Student's t-test (**P* < 0.05, ***P* < 0.01, ****P* < 0.001, and *****P* < 0.0001; Ns: no significance).

transforming growth factor-β (TGF-β) signaling pathway, cell cycle signaling pathway, microRNAs in cancer, and P53 signaling pathway (Fig. S14(a) in the ESM). Energy metabolism primarily affects oxidative phosphorylation, reactive oxygen species, glutathione metabolism, and glycolysis/gluconeogenesis signaling pathways (Fig. S14(b) in the ESM). Heat map results of differentially expressed genes indicate decreased expression of genes associated with oxidative phosphorylation and glycolysis (such as *Gapdh, Hif-1α, Hk2*, *Pfk2*, and *Pck2*), increased expression of pro-apoptotic genes (*P53, Bik, Bax, Bak*, and *Aen*), and increased expression of genes promoting cell cycle progression (such as *p21, Atm, Arf*) (Fig. 5(c)). Next, we further evaluated the changes in oxidative phosphorylation (OXPHOS) and glycolysis in BxPC3 cells treated with Vir-Z@R using the Seahorse assay. As shown in Figs. S15(a) and S15(d) in the ESM, Vir-Z@R induced an approximately 55% reduction in glycolysis and a 70% decrease in basal respiration, which were measured by the extracellular acidification rates (ECAR) and oxygen consumption rates (OCR) respectively using a seahorse-based analysis. These findings further confirm that Vir-Z@R modulates tumor cell metabolism by inhibiting both OXPHOS and glycolysis. These results suggested that the Vir-Z@R-induced restoration of P53 levels in cells predominantly triggers tumor cell death via apoptosis, cell cycle arrest, and disruption of energy metabolism pathways.

To further elucidate the *in vitro* antitumor mechanisms of Vir-Z@R in BxPC3 cells, we conducted WB studies to investigate the effects of P53 on apoptosis, the cell cycle, and energy metabolism pathways. As shown in Fig. 5(d), Vir-Z@R decreased the expression of the anti-apoptotic protein BCL-2 and efficiently activated PUMA to initiate the cleaved caspase-9 (C-CAS9) and the cleaved caspase-3 (C-CAS3)–induced apoptosis pathway. We also investigated the signaling pathways involved in cell cycle regulation by evaluating the cell cycle–related proteins in BxPC3 cells (Fig. 5(d) and Fig. S16 in the ESM). The restoration of P53 functions by Vir-Z@R resulted in the up-regulation of p21, blocking the cell cycle at the G1 and G2 phase. Remarkably, although Zn^{2+} elevates ROS, our data revealed no significant downregulation of other tumor-suppressor proteins (e.g., p53 upregulated modulator of apoptosis (PUMA), Cyt C, C-CAS3, C-CAS9 and p21) or housekeeping proteins (e.g., β-actin). This suggests that Zn^{2+}-mediated ROS levels released by Vir-ZIF are finely tuned to preferentially destabilize Mutp53 without widespread proteotoxicity. We further confirmed the alteration in the energy metabolism pathway through TEM analysis of mitochondrial morphology. Specifically, we observed an increased number of swollen mitochondria (yellow arrows) in the cytoplasm of BxPC3 cells after treatment with Vir-Z@R (Fig. 5(e)), which was recognized as a typical characteristic of mitochondrial damage [33, 34]. Correspondingly, ATP levels in Vir-Z@R group (2.3%) displayed a significant decrease than that of LNP-mRNA and Vir-ZIF groups (48.7% and 55.2%), respectively (Fig. 5(f)).

Taken together, Vir-Z@R activates downstream apoptosis pathways by restoring P53 in tumor cells and induces P53 mutant tumor cells death through synergistic damage to mitochondrial energy metabolism.

2.5 *In vivo* biological distribution and basic properties of Vir-Z@R in P53-mutated tumor

Encouraged by the above results, we established BxPC3 subcutaneous tumor model in nude mice to evaluate the antitumor efficacy of Vir-Z@R *in vivo*. As a prelude to cancer therapeutic study, we carried out preliminary evaluation on the tissue distribution and pharmacokinetics of the Vir-Z@R. As shown in Fig. 6(a), compared with free *P53* mRNA and Z@R group, RBCM-Z@R exhibited higher tumor accumulation after 3 h post-injection, which could be ascribed to RBCM-mediated prolonged circulation. Furthermore, a conspicuous accumulation of Vir-Z@R was detected at the tumor site after 1 h, with a subsequent gradual increase over time (Fig. 6(b)). The accumulation reached its peak at 24 h post-injection, indicating robust tumor targeting by Vir-Z@R (Fig. 6(c)). Meanwhile, ICP-MS was carried out to analyze the Zn content further quantitatively in major organs and tumor tissue. As expected, Vir-Z@R could be also effectively enriched in tumor sites (Fig. 6(d)), which lays the foundation for subsequent induction of reactive oxygen species production. Next, we evaluated pharmacokinetic (PK) parameters by administering Cy5-mRNA, Z@R, RBCM-Z@R and Vir-Z@R into healthy BALB/c nude mice via the tail vein. As shown in Fig. 6(e), free mRNA was rapidly cleared with a dramatic decrease to approximately 10% after 20 min. In contrast, Z@R demonstrated prolonged mRNA circulation, with over 30% of the Cy5-*P53* mRNA still circulating after 60 min. After 4 h, nearly 40% of Vir-Z@R was still detectable, whereas most free mRNA was cleared within 1 h. This result indicates that the construction of virus-mimic nanocarriers prolongs the blood circulation time of RNA, potentially improving its bioavailability.

To verify the feasibility of the virus-mimic nanoparticle system for delivering mRNA and expressing proteins *in vivo*, various nanoparticles loaded with luciferase (Luc) mRNA were intratumorally injected into BxPC3 tumor-bearing mice as the tumor model, and the ability of these carriers to express proteins *in vivo* was examined through bioluminescence imaging. As shown in Fig. 6(f) and Fig. S17 in the ESM, free Luc mRNA and Z@R(Luc) nanoparticles were rapidly metabolized *in vivo* and failed to effectively express the target protein. However, after modification with RBCM, RBCM-Z@R(Luc) nanoparticles were able to accumulate at the tumor site and successfully express luciferase. Furthermore, after further modification with functional peptides RGD and L17E, Vir-Z@R(Luc) exhibited stronger luciferase expression at the tumor site compared to RBCM-Z@R(Luc), reaching peak expression levels 24 h after intravenous injection. These results indicated that Vir-Z@R(Luc) displayed good tumor accumulations and anticipative drug release behavior on the tumor site.

2.6 *In vivo* therapeutic effect of Vir-Z@R in P53-mutated tumor

Next, we commenced to investigate the specific anti-tumor capacity of Vir-Z@R in BxPC3 tumor-bearing mouse model. To evaluate the *in vivo* anti-tumor effect of Vir-Z@R, BxPC3 tumor-bearing mice were randomly divided into four groups (n = 8 per group), and then treated with saline, LNP-mRNA, Vir-ZIF and Vir-Z@R by tail intravenous injection. As illustrated in Fig. 7(a), all formulations were administered every three days until day 21, during which tumor volume and body weight were meticulously recorded from day 0 to 21. Subsequently, at the culmination of the 21-day treatment period, all mice underwent euthanasia to facilitate the retrieval of tumor tissues. This step is depicted in Fig. 7(b), where the photographs of *ex vivo* tumor tissues for Vir-Z@R conspicuously substantiated the efficacy of *in vivo* tumor inhibition.

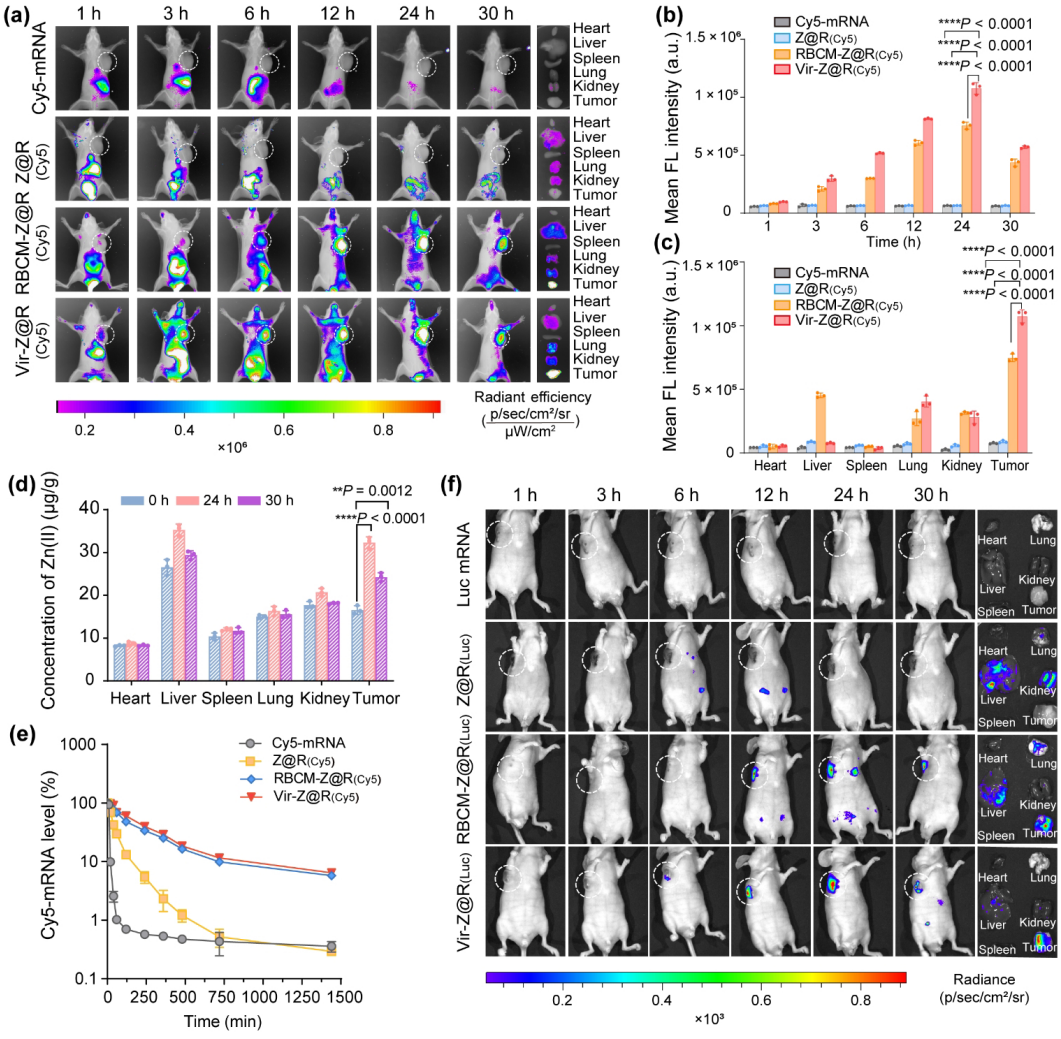

Figure 6 Tissue distribution and *in vivo* functionality of Vir-Z@R in mice. (a) Optical imaging of BxPC3 tumor-bearing mice and major tissues under different treatments over various time periods. (b) Quantitative analysis of tumor fluorescence intensity of BxPC3 tumor bearing mice model after tail vein with different treatments for different time periods, $n = 3$. (c) *Ex vivo* tissue quantitative analysis of Cy5 fluorescence intensity of BxPC3 tumor-bearing mice model at 30 h post injection with different treatment, $n = 3$. (d) The Zn(II) levels in major organs and tumor after intravenous administration of Vir-Z@R for 0, 24 and 30 h, as measured by ICP-MS. (e) Circulation profile of free Cy5-mRNA, Z@R(Cy5), RBCM- Z@R(Cy5) and Vir-Z@R(Cy5) (mRNA dose: 0.75 mg/kg) ($n = 5$) after i.v. administration. (f) *In vivo* expression and biodistribution (measured by Luc fluorescence) of Luc mRNA and Luc mRNA-carrying nanoparticles (Z@R, RBCM-Z@R, and Vir-Z@R) in mice following intravenous injection. Data in (b)–(e) are presented as mean ± SD. Statistical differences between the two groups were determined using unpaired two-tailed Student's t-test (*$P < 0.05$, **$P < 0.01$, ***$P < 0.001$, and ****$P < 0.0001$; Ns: no significance).

As shown in Fig. S18 in the ESM, treatment with saline and LNP-mRNA alone had almost no effect on tumor growth. In contrast, treatment with Vir-ZIF and Vir-Z@R significantly suppressed tumor growth, reducing tumor volume by 51.77% and 93.11% tumor weight by 40% and 93.46%, respectively (Fig. 7(c) and Fig. S18 in the ESM). Together, Vir-Z@R treatment showed the most powerful anti-tumor effect and markedly improved the survival rate and prolonged the survival time of the mice (Fig. 7(d)).

To further assess the apoptosis rate within the tumors of treated mice, we performed hematoxylin & eosin (H&E) staining, transferase-mediated dUTP nick end-labeling (TUNEL) fluorescence staining and Ki-67 immunofluorescence staining. H&E staining showed more necrotic areas in the tumor tissue in the Vir-Z@R group (Fig. 7(e)). The highest apoptotic index (green fluorescence in TUNEL images) and lowest proliferative index (red fluorescence in Ki-67 images) were also observed in the Vir-Z@R group, further demonstrating that the anti-tumor efficacy of Vir-Z@R, with increasing cell apoptosis upon treatment with Vir-Z@R. Given the above results, in P53-mutant BxPC3, Vir-Z@R possessed the greatest antitumor efficacy.

To further prove the synergistic effect of Vir-Z@R, we assessed the levels of Wtp53 and total-P53 in tumor tissues of different treatment groups through WB. As shown in the Figs. 8(a) and 8(b), compared to the other groups, the Vir-Z@R group significantly increased the expression level of Wtp53 and total P53 within tumor cells. Meanwhile, Vir-ZIF significantly reduced the total P53 level, which may because of that Zn(II) degrade Mutp53 in BxPC3. Notably, immunofluorescence results showed Vir-Z@R treatment resulted in higher levels of ROS and the apoptotic protein caspase 3 (Figs. 8(c) and 8(d)). Intratumoral ATP levels were further measured. ATP levels after treatment of Vir-Z@R were obviously declined by 72.5%, which was much lower than that of other groups (Fig. S19 in the ESM). These results confirmed that Vir-Z@R, after restoring P53, induces tumor cell death through multiple pathways

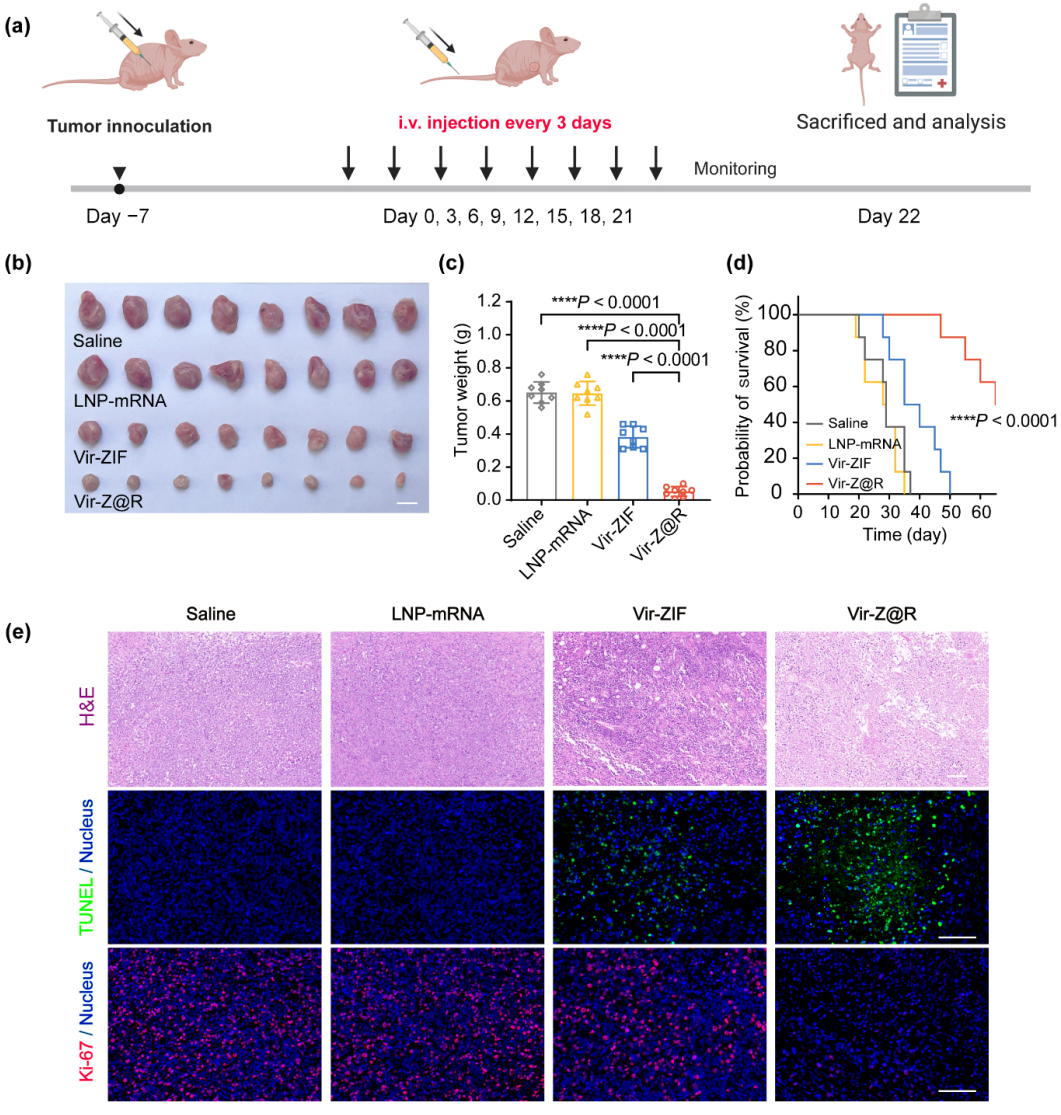

Figure 7 The *in vivo* anticancer efficacy of Vir-Z@R. (a) A schematic showing treatment schedule for the subcutaneous pancreatic cancer mouse model (n = 8). (b) Photographs of tumors excised from mice with indicated treatments on day 22 (n = 8). Scale bar: 1 cm. (c) Weight of tumors resected from mice with indicated treatments on day 22 (n = 8). (d) Survival curves of BxPC3 tumor bearing mice with indicated treatments during the 65-day observation period. (e) H&E staining, TUNEL and Ki-67 immunofluorescence staining of tumor sections from subcutaneous BxPC3 tumor bearing mice with indicated treatments on day 22. Scale bar: 100 μm. Data in (c) and (d) are presented as mean ± SD. Statistical differences between the two groups were determined using unpaired two-tailed Student's t-test (*P < 0.05, **P < 0.01, ***P < 0.001, and ****P < 0.0001; Ns: no significance).

and mechanisms. Collectively, the above results demonstrated that Vir-Z@R by restoring P53 in tumor cells, repair the natural mechanism of inhibiting cancer, amplify oxidative stress, and inhibit energy metabolism of tumor cells synergistically induce cell death.

2.7 Biosafety evaluation of Vir-Z@R *in vivo*

Biosafety is always the priority in tumor treatment. To assess the *in vivo* safety of Vir-Z@R, we monitored mouse weight throughout the animal studies mentioned above and collected blood as well as major organs (e.g., heart, kidneys, liver, lung, and spleen) at the conclusion of these investigations. As illustrated in Fig. S20 in the ESM, the overall body weight of mice receiving all nano-formulations exhibited a consistent increase throughout the entire treatment period. Hematological analysis was conducted with utilizing serum biochemistry and whole blood panel tests. As depicted in Fig. S21 in the ESM, no significant alterations was observed in any hematological parameter among the groups, suggesting minimal adverse effects associated with Vir-Z@R. We also examined the major organs by H&E staining. Histological analyses revealed no obvious abnormality and no differences in the main organs among the treatment groups, further demonstrating the bio-safety of Vir-Z@R for application *in vivo* (Fig. S22 in the ESM).

3 Conclusions

The P53 tumor suppressor is the most frequently altered gene in human cancers, and has been a major focus of oncology research. The P53 protein is a transcription factor that can activate the expression of multiple target genes and play critical roles in regulating cell cycle, apoptosis, and genomic stability, and is widely regarded as the "guardian of the genome". Accumulating evidence

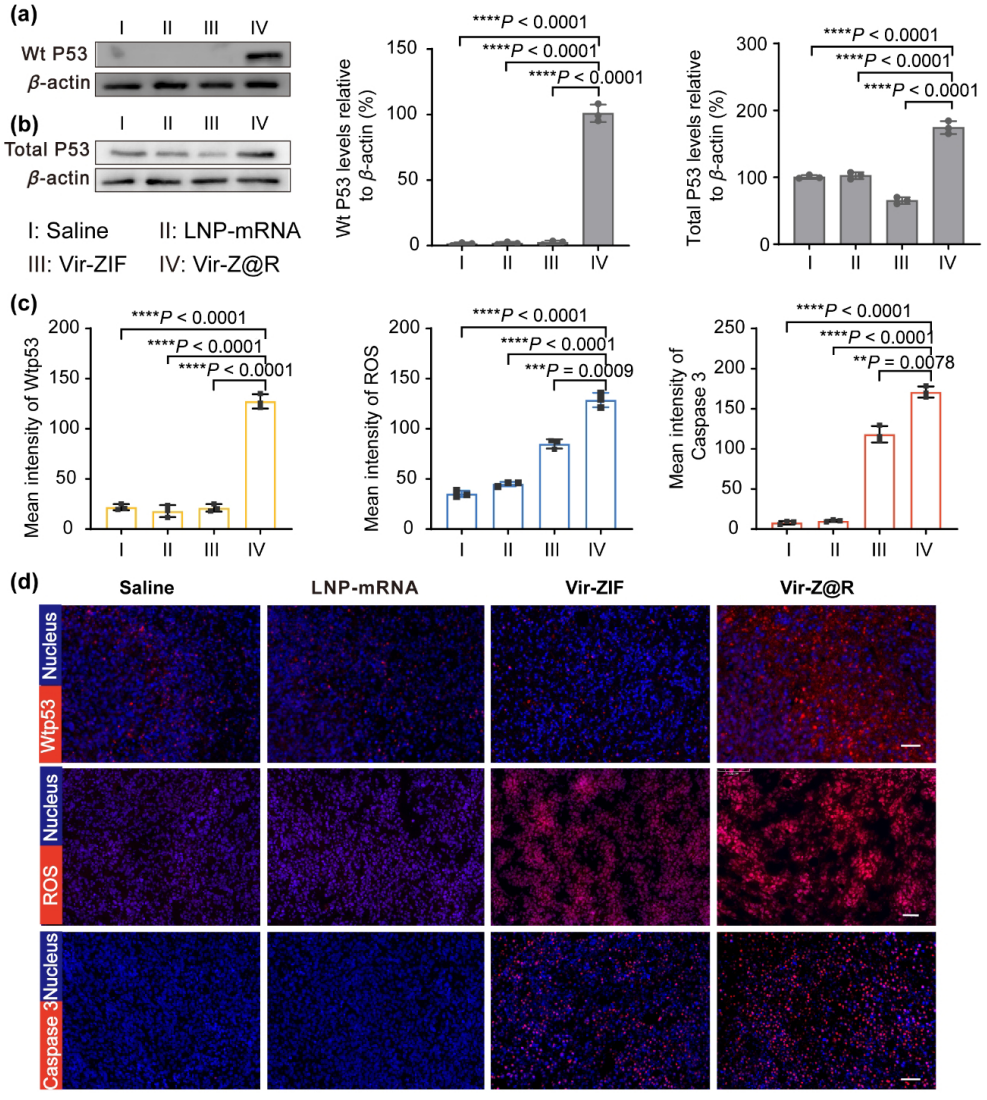

Figure 8 The *in vivo* anticancer mechanism of Vir-Z@R. (a) Western blot analysis of WtP53 and (b) total P53 in the excised tumor tissues after indicated treatments. *β*-actin was used as the loading control. (c) The immunofluorescence images and (d) quantitative analysis of WtP53 protein, ROS, and Caspase 3 in tumor sections from subcutaneous pancreatic cancer-bearing mice treated as indicated on day 22. Scale bar: 50 μm. Data in (a)–(c) are presented as mean ± SD. Statistical differences between the two groups were determined using unpaired two-tailed Student's t-test (*$P < 0.05$, **$P < 0.01$, ***$P < 0.001$, and ****$P < 0.0001$; Ns: no significance).

has shown that P53 also regulates cell metabolism, ferroptosis, tumor microenvironment, autophagy and so on, all of which contribute to tumor suppression. Mutations in P53 not only impair its tumor suppressor function, but also confer oncogenic properties to P53 mutants. Since P53 is mutated and inactivated in most malignant tumors, it has been a very attractive target for developing new anti-cancer drugs. Currently, several *P53*-targeting small-molecule drugs such as APR-24, JAB-30355, and PC14586 have been developed. While these compounds have demonstrated the ability to reactivate P53's tumor-suppressive function by restoring wild-type conformation in clinical trials, their therapeutic efficacy remains restricted to specific P53 mutation subtypes (e.g., R175H for APR-246) and exhibits variable response rates (typically 30%–50% in Phase II/III studies).

mRNA strategies aimed at restoring P53 function hold the potential to overcome the bottlenecks in P53-targeted drug development, offering new hope for P53-targeted therapies. Thanks to the successful deployment of COVID-19 mRNA vaccines, LNPs have emerged as the most advanced non-viral mRNA delivery platform in clinical applications. Although previous studies have demonstrated that LNPs can deliver *P53* mRNA to *P53*-deficient tumor cells, thereby increasing P53 protein levels and restoring its tumor-suppressing functions, challenges remain in tumors harboring P53 mutations. Mutant P53 proteins not only promote tumor proliferation and metastasis through gain-of-function mechanisms, but also inhibit the function of Wtp53 via a dominant-negative effect. Furthermore, the Wtp53 protein has a short half-life in cells, making it critical to stabilize P53 to effectively restore its anti-cancer function. Based on this analysis, the key to restoring P53 functionality lies in simultaneously degrading Mutp53 proteins while increasing and stabilizing Wtp53. Zn(II) ions can bind to the DNA-binding domain of *P53*, aiding in the structural stabilization of *P53* and enhancing its transcriptional activation functions. Moreover, studies have shown that Zn(II) can induce the production of reactive oxygen species, leading to the degradation of Mutp53 proteins through the ubiquitin-proteasome pathway. However, current LNP-based *P53* mRNA delivery systems are unable to efficiently co-transport metal ions.

In conclusion, a virus-mimicking nanoparticle delivery system (Vir-Z@R) is designed for the treatment of *P53* mutant tumor. Vir-Z@R, which mimics viral structures, exhibits various functionalities including immune evasion, tumor targeting, and intracellular lysosome escape. It efficiently delivers *P53* mRNA and Zn(II) into tumor cells, facilitating effective supplementation of Wtp53 and specific degradation of Mutp53 via Zn(II)-mediated proteasomal pathways. As a result, it restores the tumor-suppressive function of Wtp53, counteracts the oncogenic effects of Mutp53, halts the cell cycle, suppresses tumor cell energy metabolism, and induces apoptosis. This multi-functional platform not only addresses the pharmacokinetic limitations of small molecule approaches like APR-246, but also advances beyond conventional mRNA therapeutics by solving the critical challenges of Mutp53 dominance and Wtp53 instability. The integrated strategy of Vir-Z@R establishes a new paradigm for P53-targeted cancer therapy with potential applications across diverse P53-mutant malignancies.

4 Experimental

4.1 Materials

Imidazole-2-carboxyaldehyde was procured from Merck, while $Zn(OAc)_2{\cdot}2H_2O$ was obtained from Aladdin. *P53* mRNA was sourced from APExBIO, Houston, USA and DSPE-PGE2000-RGD peptide was purchased from Xi'an Ruixi Biological Technology Co., Ltd (Shaanxi, China). DSPE-PGE2000-L17E was acquired from ChinaPeptides Co., Ltd (Shanghai, China), and ATP was obtained from MedChemExpress (MCE) company (HY-B2176T). Various assay kits, including the Bicinchoninic acid (BCA) Protein Assay Kit, Annexin V-FITC Apoptosis Detection Kit (KeyGEN BioTECH), and ATP Content Assay Kit, were purchased from Beijing Solarbio Science & Technology Co., Ltd. Anti-CD47 antibody was procured from Abcam (ab218810). Anti-CD41 antibody was procured from Thermo Fisher Scientific (PA5-22307). Anti-CD235*α* antibody was purchased from MyBioSource (MBS9411190). Anti-p53 antibody was procured from Abcam (ab32049). Anti-Hb antibody was procured from iReal Biotechnology (IRM018). Anti-P53 protein (Wt-P53) antibody was purchased from Beijing Biosynthesis Biotechnology Co., Ltd (Bs-0033R). Anti Cleaved Caspase 3 antibody was procured from Abcam (ab2302). Anti Cleaved Caspase 9 antibody was procured from Cell signaling technology (9501). Anti-Bcl-2 antibody was procured from Abcam (ab32124). Anti-p21 antibody was procured from Abcam (ab109199). Anti-PUMA antibody was procured from Abcam (ab9643). Anti- Cytochrome C antibody was procured from Abcam (ab133504). Anti-beta Actin antibody was procured from Abcam (ab8226). Lyso-Tracker Green and Hoechst 33342 (100×) were sourced from Yeasen Biotechnology Co., Ltd. BxPC3 Human Pancreatic Adenocarcinoma Cells was purchased from Wuhan PunoCell Life Sciences Co., Ltd (CL-0042). RAW264.7 Mouse Macrophage Cells was purchased from Wuhan PunoCell Life Sciences Co., Ltd (CL-0190). A549 Human Lung Carcinoma Cells were purchased from Wuhan PunoCell Life Sciences Co., Ltd (CL-0016). MDA-MB-231 Human Breast Adenocarcinoma Cells were purchased from Wuhan PunoCell Life Sciences Co., Ltd (CL-0150). T7 High Yield RNA Transcription kit and RNase inhibitor was purchased from Novoprotein Scientific (China). Aminoallyl-UTP was purchased from MedBio Pharmaceutical Technology Inc. CELLSAVING (Cat.No.C40100) was purchased from New Cell & Molecular Biotech. Gel Rapid Extraction Kit was procured from JiangSu CoWin Biotech (CWBIO). The total mRNA was isolated by TRIeasyTM Total RNA Extraction Reagent (10606ES60), which was purchased from Yeasen Biotechnology Co., Ltd. The qRT-PCR kit (cat. no. AQ601-01) was purchased from TransGen Biotech, Beijing, China. D-Luciferin potassium salt as purchased from J&K Scientific. CCK-8 Cell Proliferation and Cytotoxicity Assay Kit was purchased from Absin (Shanghai) Biotechnology Co., Ltd. Sparkjade ECL super was purchased from Shandong Sparkjade Biotechnology Co., Ltd. StarMarker 1kb Ladder Plus (M015) and StarStain Red Plus10000× (E110) (GenStar (Beijing, China)).

4.2 Preparation of Vir-Z@R

In a solution devoid of RNAase, 100 μg of *P53* mRNA was dissolved in 900 μL of DEPC water along with 12.3 mg of $Zn(CH_3COOH)_2{\cdot}2H_2O$ and incubated at room temperature for 5 min. Simultaneously, 18.7 mg of 2-ICA was dissolved in 4 mL of N,N-Dimethylformamide (DMF) to achieve a concentration of 48.8 mM. Following this, the 2-ICA solution was stirred at 2000 rpm for 2 min in a round-bottomed flask. Subsequently, 900 μL of the dissolved $Zn(CH_3COOH)_2{\cdot}2H_2O$ and *P53* mRNA aqueous solution was swiftly added, and stirring was continued for 10 min. After completion of the reaction, the precipitate was collected by centrifugation at 1500 rpm for 3 min. The precipitate underwent a single wash using anhydrous ethanol at 6500 rpm for 3 min, followed by two washes with diethylpyrocarbonate (DEPC) water under the same conditions, resulting in the formation of ZIF-90@RNA (Z@R). RBCM-Z@R nanoparticles were generated by combining 60 μg of RBCM with 500 μL of Z@R, followed by sequential extrusion through filter membranes with pore sizes of 800 and 450 nm. Furthermore, 1 mg of DSPE-PEG-RGD peptide and 1 mg of DSPE-PEG-L17E peptide were dissolved in 1 mL of DMF each. Subsequently, 10 μL of each dissolved RGD peptide and L17E peptide was incubated with 500 μL of RBCM-Z@R at 37 °C for 2 h. Finally, the precipitates were centrifuged at 12,000 rpm for 20 min, yielding erythrocyte membrane-coated mimetic viral nanoparticles (Vir-Z@R) modified with RGD and L17E peptides.

4.3 Determination of encapsulation efficiency of *P53* mRNA

To determine the encapsulation efficiency (EE) of *P53* mRNA in ZIF-90, Z@R containing different amounts of *P53* mRNA were prepared. EE of *P53* mRNA in Z@R was measured according to the instructions provided in the Quant-iT™ RiboGreen® RNA Reagent kit.

4.4 Peptide modification quantification

Vir-Z@R nanoparticles were prepared by engineering the modification of RBCM using fluorescent isothiocyanate fluorescein isothiocyanate-labeled RGD peptide and Cy5-labeled L17E peptide. Using a Multifunctional Microplate Reader (Agilent SH1M2, Agilent Technologies USA), the fluorescence intensity of the RGD peptide and L17E peptide was measured to calculate the amount of their modification on the Vir-Z@R surface.

4.5 Cell culture

The BxPC3 human pancreatic cancer cell line was cultured in RPMI 1640 (Procell Life Science&Technology Co., Ltd.), supplemented with 10% (v/v) FBS (Lonsera, Suzhou Shuangru

Biology Science& Technology Co., Ltd), penicillin (100 U/mL), and streptomycin (100 μg/mL). Meanwhile, the A549 human non-small cell lung cancer cell line and the MDA-MB-231 human breast cancer cell line were cultured in Dulbecco's modified eagle medium (DMEM), supplemented with 10% (v/v) fetal bovine serum, penicillin (100 U/mL), and streptomycin (100 μg/mL). Subsequently, these cell lines were incubated in a controlled environment at 37 °C, 5% CO_2, and 90% humidity.

4.6 Cellular uptake experiment

Raw264.7 and BxPC3 cells were co-incubated with drug-containing medium containing naked *P53* mRNA, Z@R, L17E-RBCM-Z@R, and Vir-Z@R (in which the concentration of *P53* mRNA was 20 ng/μL) for 4 h. Subsequently, samples of cells from each group were collected and analyzed using flow cytometry (Challenbio FongCyte™, Beijing Challen Biotechnology Co., Ltd, China), and the resulting data were analyzed by FlowJo V10 software Processing.

4.7 Endosomal escape experiment

To visualize the lysosomal escape of nanoparticles in cells, RGD-RBCM-Z@R and Vir-Z@R nanoparticles prepared with Cy5-*P53* mRNA (where the concentration of *P53* mRNA was 20 ng/μL) were incubated with BxPC3 cells for 0, 1, 2, and 4 h, respectively, and then washed twice with PBS. LysoTracker Green (50 nM) working solution was added, and the lysosomes were labeled by co-incubation with the cells at 37 °C for 8 min. Finally, the lysosomes were stained with Hoechst 33342 working solution protected from light for 10 min, and the lysosomal escape of the nanoparticles was observed and recorded using Leica DMi8 automated THUNDER imager (Leica Microsystems CMS GmbH).

4.8 Examination of intracellular protein expression capacity

BxPC3 cells were co-incubated with EGFP mRNA, Z@R(EGFP), RBCM-Z@R(EGFP) and Vir-Z@R(EGFP) solutions (all at a concentration of 20 ng/μL of EGFP mRNA) for 24 h. At the end of incubation, the drug-containing medium was removed, and the cells were washed three times with PBS. After staining with Hoechst 33342 working solution for 10 min and washing the cells with PBS for three times, the EGFP protein expression was observed using Leica DMi8 automated THUNDER imager and photographed. And the percentage of EGFP positive cells was analyzed by Challenbio FongCyte™ (Beijing Challen Biotechnology Co., Ltd).

4.9 Examination of intracellular zinc ion levels

BxPC3 cells were incubated with Control, LNP-mRNA, Vir-ZIF and Vir-Z@R for 4 h. At the end of the incubation, cells were digested to collect the cell precipitate and counted. An equal amount of cell precipitate was incubated with 3 g/mL of HNO_3 for 12 h. 30% H_2O_2 solution was added and mixed, and the cells were continuously heated in a water bath for 4 h until the precipitate was completely digested. After cooling to room temperature, 2% HNO_3 solution was added and diluted by mixing, and the volume was fixed to 10 mL, and the content of zinc ions was detected by ICP-MS.

4.10 Determination of Wtp53 by western blot

In the experiment, BxPC3 cells were treated with culture media containing various substances: Control, LNP-mRNA, Vir-ZIF, and Vir-Z@R for 8 h. Following this co-incubation, the cells were rinsed twice with PBS and subsequently incubated with fresh culture medium for an additional 24 h. After this period, the cells were harvested by trypsin digestion and centrifuged at 1000 rpm for 5 min at 4 °C to obtain cell pellets. Total protein content was assessed using the BCA protein assay. The protein samples were then mixed with loading buffer and heated at 100 °C for 5 min. Subsequently, 40 μg of protein from each sample was separated on a 12% SDS-polyacrylamide gel and electro transferred onto a polyvinylidene difluoride (PVDF) membrane. The PVDF membrane was blocked with 5% non-fat dry milk in Tris-buffered saline with Tween-20 (TBST) for 2 h to prevent non-specific binding. After blocking, the membrane was incubated with primary antibodies for 4 h, followed by incubation with secondary antibodies for 2 h. Protein bands were visualized using Amersham ImageQuant 800 (Cytiva Sweden AB). To quantify protein expression levels, the intensity of the protein bands was normalized to β-actin levels. Semi-quantitative analysis of band intensity was performed using Image J software.

4.11 Cell viability assay

BxPC3 cells were treated with Vir-ZIF and Vir-Z@R, respectively, for 8 h. After the incubation was completed, the cells were washed twice with PBS, and 10 μL of CCK-8 solution was added to each well, and then the cells were incubated for another 1 h. The absorbance (OD) values of the cells were then measured using an enzyme counter at 450 nm in each well.

4.12 Experimental animals

The animals used in this study were 5–6 week-old male BALB/c nude mice, purchased from Beijing HFK Bioscience Co., Ltd. The experimental animal production license number is SCXK (Jing) 2019-0004, and the quality certificate number is No. 110322231102502182. The ethical review approval number is yxyllsc20230096 (School of Pharmacy Animal Ethics Committee, Zhengzhou University). The experimental animal facility license number is SYXK (Yu) 2018-0004. The feed production license number is SCXK (Jing) 2019-0010.

4.13 *In vivo* therapeutic efficacy and mechanism of Vir-Z@R

To evaluate the *in vivo* therapeutic efficacy and underlying mechanisms of Vir-Z@R, a total of 64 tumor-bearing mice with tumor volumes approximately 100 mm^3 were selected and randomly divided into four groups using a random number method: (I) Saline group (200 μL, physiological saline), (II) LNP-mRNA group (200 μL, containing 13 μg of *P53* mRNA), (III) Vir-ZIF group (200 μL, containing 252 μg of ZIF-90), and (IV) Vir-Z@R group (200 μL, containing 252 μg of ZIF-90 and 13 μg of *P53* mRNA), with 16 mice in each group. On days 0, 3, 6, 9, 12, 15, 18, and 21, mice in the Saline group received tail vein injections of 200 μL physiological saline, while the other groups received their respective formulations through tail vein injections. After the treatment period, 8 mice from each group were randomly selected and euthanized using cervical dislocation. Organs including the heart, liver, spleen, lungs, kidneys, and tumor tissues were harvested for subsequent investigation of the antitumor effects and mechanisms. All tissues were fixed in 4% paraformaldehyde, embedded in paraffin, and subjected to H&E staining.

4.14 *In vivo* imaging

Twelve BxPC3 hormonal male nude mice with tumor volume of about 100 mm^3 were taken and randomly divided into four groups: (I) naked Cy5-mRNA, (II) Z@R(Cy5), (III) RBCM-Z@R(Cy5), and (IV) Vir-Z@R(Cy5), with three mice in each group. Nude mice in each group were given Cy5-labeled mRNA, Z@R(Cy5), RBCM-Z@R(Cy5), and Vir-Z@R(Cy5) by tail vein injection for targeting evaluation, respectively, where the mRNA dose was 750 μg/kg (mRNA/animal body weight). *In vivo* imaging was performed in each group of tumor-bearing nude mice using the *in vivo* imaging system (IVIS) at different time points (1, 3, 6, 12, 24, and 30 h) after intravenous drug administration. The mice were also euthanized 30 h after drug injection, and major organs (heart, liver, spleen, lungs, kidneys) and tumor tissues were dissected for *in vitro* fluorescence imaging analysis.

4.15 Analyzing Vir-Z@R's *in vivo* protein expression ability

BxPC3 hormonal male nude mice were randomly divided into four groups: (I) Luc-mRNA, (II) Z@R(Luc), (III) RBCM-Z@R(Luc), and (IV) Vir-Z@R(Luc), with three mice in each group. Nude mice in each group were given Z@R, RBCM-Z@R, and Vir-Z@R loaded with luciferase (Luc) mRNA by tail vein injection, respectively, where the mRNA dose was 750 μg/kg (mRNA/animal body weight). The nude mice were imaged *in vivo* using the IVIS imaging system at different time points (3, 6, 12, 24, and 30 h) after intravenous drug administration. And the mice were euthanized 30 h after drug injection, and major organs (heart, liver, spleen, lung, kidney) and tumor tissues were dissected for *in vitro* fluorescence imaging.

4.16 Analyzing Vir-Z@R's *in vivo* zinc ion production ability

When the tumor volume of BxPC3 hormonal male nude mice reached 100 mm^3, nine hormonal nude mice were randomly selected and divided into three groups: (I) 0 h, (II) 24 h, and (III) 30 h, with three mice in each group, all of which were injected with Vir-Z@R (200 μL, ZIF-90: 252 μg) via tail vein. At predetermined time points (0, 24 and 30 h), the mice were euthanized, and heart, liver, spleen, lung, kidney, and tumor tissues were collected. After washing the tissues, excess water was absorbed with filter paper and the tissues were minced into test tubes. Subsequently, HNO_3 (3 mL/g) was added to the test tubes and acid digested at room temperature for 12 h. After that, 30% H_2O_2 (0.6 mL/mg) was added, and the test tubes were heated in a water bath for 4 h to completely digest the tissues. After cooling to room temperature, 2% HNO_3 was added and fixed to 10 mL. Finally, the zinc ion concentration was detected using ICP-MS.

4.17 Statistical analysis

All data in this paper were treated using a Student's t-test, and statistical analyses were performed by GraphPad software. All of results were presented by mean ± SD. *P* values: $^*P < 0.05$, $^{**}P < 0.01$, $^{***}P < 0.001$ and $^{****}P < 0.0001$.

Electronic Supplementary Material: Supplementary material (optimization of preparation conditions for Z@R, the stability of Vir-Z@R, the cytobehavioral studies of Vir-Z@R, study on ubiquitination of Vir-ZIF, studies on glycolysis at Vir-Z@R, safety study of Vir-Z@R) is available in the online version of this article at https://doi.org/10.26599/NR.2025.94907529.

Data availability

All data needed to support the conclusions in the paper are presented in the manuscript and the Electronic Supplementary Material. Additional data related to this paper may be requested from the corresponding author upon request.

Acknowledgements

This project is supported by the National Natural Science Foundations of China (Nos. 22122409, 22377110, and 82402749). Henan Province Fund for Cultivating Advantageous Disciplines (No. 222301420019). Authors thank Modern Analysis and Computing Center of Zhengzhou University for technical assistance. The authors would like to thank Shiyanjia Lab (www.shiyanjia.com) for the TEM analysis. The animal study protocol was approved by the Institutional Animal Care and Use Committee at Zhengzhou University.

Declaration of competing interest

The authors declare no competing financial interest.

Author contribution statement

Y. L.: Writing — review & editing, writing — original draft, conceptualization. C. L. X.: Writing — review & editing, methodology, investigation. J. G. Z.: Investigation methodology. S. G. L.: Methodology. M. H. Y.: Investigation, methodology. Y. C. L.: Supervision, methodology. H. G.: Writing — review & editing, funding acquisition. K. X. Z.: Writing — review & editing, conceptualization, funding acquisition.

Informed consent

Not applicable.

Ethics statement

The animal experiments were carried out following the guidelines of the Zhengzhou University Institutional Committee for the Care and Use of Laboratory Animals and were approved by the Committee on Ethical Use of Animals of Zhengzhou University (Ethical code: 110322231102502182).

Use of AI statement

None.

References

[1] Hassin, O.; Oren, M. Drugging p53 in cancer: One protein, many targets. *Nat. Rev. Drug Discov.* **2023**, *22*, 127–144.

[2] Janic, A.; Valente, L. J.; Wakefield, M. J.; Di Stefano, L.; Milla, L.; Wilcox, S.; Yang, H. Y.; Tai, L.; Vandenberg, C. J.; Kueh, A. J. et al. DNA repair processes are critical mediators of p53-dependent tumor suppression. *Nat. Med.* **2018**, *24*, 947–953.

[3] Miller, J. J.; Gaiddon, C.; Storr, T. A balancing act: Using small molecules for therapeutic intervention of the p53 pathway in cancer. *Chem. Soc. Rev.* **2020**, *49*, 6995–7014.

[4] Levine, A. J. p53: 800 million years of evolution and 40 years of discovery. *Nat. Rev. Cancer* **2020**, *20*, 471–480.
[5] Bykov, V. J. N.; Eriksson, S. E.; Bianchi, J.; Wiman, K. G. Targeting mutant p53 for efficient cancer therapy. *Nat. Rev. Cancer* **2018**, *18*, 89–102.
[6] Wang, H. L.; Guo, M.; Wei, H. D.; Chen, Y. H. Targeting p53 pathways: Mechanisms, structures and advances in therapy. *Sig. Transduct. Target. Ther.* **2023**, *8*, 92.
[7] Efe, G.; Rustgi, A. K.; Prives, C. p53 at the crossroads of tumor immunity. *Nat. Cancer* **2024**, *5*, 983–995
[8] Qian, J. Y.; Zhang, W. B.; Wei, P. F.; Yao, G. Y.; Yi, T. X.; Zhang, H.; Ding, H.; Huang, X. W.; Wang, M. M.; Song, Y. et al. Enhancing chemotherapy of p53-mutated cancer through ubiquitination-dependent proteasomal degradation of mutant p53 proteins by engineered ZnFe-4 nanoparticles. *Adv. Funct. Mater.* **2020**, *30*, 2001994.
[9] Xiao, Y. L.; Chen, J.; Zhou, H.; Zeng, X. D.; Ruan, Z. P.; Pu, Z. Y.; Jiang, X. Y.; Matsui, A.; Zhu, L. L.; Amoozgar, Z. et al. Combining p53 mRNA nanotherapy with immune checkpoint blockade reprograms the immune microenvironment for effective cancer therapy. *Nat. Commun.* **2022**, *13*, 758.
[10] Giacomelli, A. O.; Yang, X. P.; Lintner, R. E.; McFarland, J. M.; Duby, M.; Kim, J.; Howard, T. P.; Takeda, D. Y.; Ly, S. H.; Kim, E. et al. Mutational processes shape the landscape of *TP53* mutations in human cancer. *Nat. Genetics* **2018**, *50*, 1381–1387.
[11] Wang, Z. L.; Burigotto, M.; Ghetti, S.; Vaillant, F.; Tan, T.; Capaldo, B. D.; Palmieri, M.; Hirokawa, Y.; Tai, L.; Simpson, D. S. et al. Loss-of-function but not gain-of-function properties of mutant TP53 are critical for the proliferation, survival, and metastasis of a broad range of cancer cells. *Cancer Discov.* **2024**, *14*, 362–379.
[12] Alexandrova, E. M.; Yallowitz, A. R.; Li, D.; Xu, S.; Schulz, R.; Proia, D. A.; Lozano, G.; Dobbelstein, M.; Moll, U. M. Improving survival by exploiting tumour dependence on stabilized mutant p53 for treatment. *Nature* **2015**, *523*, 352–356.
[13] Zhao, M.; Wang, T. X.; Gleber-Netto, F. O.; Chen, Z.; McGrail, D. J.; Gomez, J. A.; Ju, W. T.; Gadhikar, M. A.; Ma, W. C.; Shen, L. et al. Mutant p53 gains oncogenic functions through a chromosomal instability-induced cytosolic DNA response. *Nat. Commun.* **2024**, *15*, 180.
[14] Liang, Y.; Han, W. S.; Xu, C. L.; Wang, J. J.; Zhang, J. G.; An, J. Y.; Liu, W.; Liu, J. J.; Zhang, Z. Z.; Shi, J. J. et al. Cascade-responsive "oxidative stress amplifiers" simultaneously destroy lysosomes and co-deliver CRISPR/Cas9 to enhance oxidative damage in tumor. *Adv. Funct. Mater.* **2023**, *33*, 2301256.
[15] Zhang, Y. J.; Huang, X. W.; Wang, L. S.; Cao, C.; Zhang, H.; Wei, P. F.; Ding, H.; Song, Y.; Chen, Z. Y.; Qian, J. Y. et al. Glutathionylation-dependent proteasomal degradation of wide-spectrum mutant p53 proteins by engineered zeolitic imidazolate framework-8. *Biomaterials* **2021**, *271*, 120720.
[16] Wang, J. P.; Qu, C.; Shao, X. Y.; Song, G. Q.; Sun, J. Y.; Shi, D. H.; Jia, R.; An, H. L.; Wang, H. J. Carrier-free nanoprodrug for p53-mutated tumor therapy via concurrent delivery of zinc-manganese dual ions and ROS. *Bioact. Mater.* **2023**, *20*, 404–417.
[17] Garufi, A.; Pucci, D.; D'Orazi, V.; Cirone, M.; Bossi, G.; Avantaggiati, M. L.; D'Orazi, G. Degradation of mutant p53H175 protein by Zn(II) through autophagy. *Cell Death Dis.* **2014**, *5*, 1271.
[18] Miller, J. J.; Kwan, K.; Gaiddon, C.; Storr, T. A role for bioinorganic chemistry in the reactivation of mutant p53 in cancer. *JBIC J. Biol. Inorg. Chem.* **2022**, *27*, 393–403.
[19] Ng, K. W.; Khoo, S. P.; Heng, B. C.; Setyawati, M. I.; Tan, E. C.; Zhao, X. X.; Xiong, S. J.; Fang, W. R.; Leong, D. T.; Loo, J. S. C. The role of the tumor suppressor p53 pathway in the cellular DNA damage response to zinc oxide nanoparticles. *Biomaterials* **2011**, *32*, 8218–8225.
[20] Lei, Y. T.; Zhang, G. H.; Zhang, Q. L.; Yu, L.; Li, H.; Yu, H. L.; He, Y. Visualization of gaseous iodine adsorption on single zeolitic imidazolate framework-90 particles. *Nat. Commun.* **2021**, *12*, 4483.
[21] Wu, S. X.; Zhang, K. X.; Liang, Y.; Wei, Y. B.; An, J. Y.; Wang, Y. F.; Yang, J. L.; Zhang, H. L.; Zhang, Z. Z.; Liu, J. J. et al. Nano-enabled tumor systematic energy exhaustion via zinc (II) interference mediated glycolysis inhibition and specific GLUT1 depletion. *Adv. Sci.* **2022**, *9*, 2103534.
[22] Deng, J. J.; Wang, K.; Wang, M.; Yu, P.; Mao, L. Q. Mitochondria targeted nanoscale zeolitic imidazole framework-90 for ATP imaging in live cells. *J. Am. Chem. Soc.* **2017**, *139*, 5877–5882.
[23] Yang, X. T.; Tang, Q.; Jiang, Y.; Zhang, M. N.; Wang, M.; Mao, L. Q. Nanoscale ATP-responsive zeolitic imidazole framework-90 as a general platform for cytosolic protein delivery and genome editing. *J. Am. Chem. Soc.* **2019**, *141*, 3782–3786.
[24] Yu, M.; Zeng, W. W.; Ouyang, Y. Q.; Liang, S.; Yi, Y. F.; Hao, H. S.; Yu, J. Y.; Liu, Y.; Nie, Y. C.; Wang, T. Q. et al. ATP-exhausted nanocomplexes for intratumoral metabolic intervention and photoimmunotherapy. *Biomaterials* **2022**, *284*, 121503.
[25] Yang, J. L.; Wang, F.; Lu, Y.; Qi, J.; Deng, L. F.; Sousa, F.; Sarmento, B.; Xu, X. Y.; Cui, W. G. Recent advance of erythrocyte-mimicking nanovehicles: From bench to bedside. *J. Controlled Release* **2019**, *314*, 81–91.
[26] Ma, H. W.; Yang, Y. H.; Nie, T. J.; Yan, R.; Si, Y.; Wei, J.; Li, M. Y.; Liu, H.; Ye, W.; Zhang, H. et al. Disparate macrophage responses are linked to infection outcome of Hantan virus in humans or rodents. *Nat. Commun.* **2024**, *15*, 438.
[27] Akishiba, M.; Takeuchi, T.; Kawaguchi, Y.; Sakamoto, K.; Yu, H. H.; Nakase, I.; Takatani-Nakase, T.; Madani, F.; Gräslund, A.; Futaki, S. Cytosolic antibody delivery by lipid-sensitive endosomolytic peptide. *Nat. Chem.* **2017**, *9*, 751–761.
[28] Omo-Lamai, S.; Zamora, M. E.; Patel, M. N.; Wu, J. C.; Nong, J.; Wang, Z. C.; Peshkova, A.; Majumder, A.; Melamed, J. R.; Chase, L. S. et al. Physicochemical targeting of lipid nanoparticles to the lungs induces clotting: Mechanisms and solutions. *Adv. Mater.* **2024**, *36*, 2312026.
[29] Huang, X. W.; Cao, Z. Y.; Qian, J. Y.; Ding, T.; Wu, Y. X.; Zhang, H.; Zhong, S. Q.; Wang, X. L.; Ren, X. G.; Zhang, W. et al. Nanoreceptors promote mutant p53 protein degradation by mimicking selective autophagy receptors. *Nat. Nanotechnol.* **2024**, *19*, 545–553.
[30] Sun, L.; Gao, H. B.; Wang, H.; Zhou, J. W.; Ji, X. R.; Jiao, Y. X.; Qin, X. J.; Ni, D. L.; Zheng, X. P. Nanoscale metal-organic frameworks-mediated degradation of mutant p53 proteins and activation of cGAS-STING pathway for enhanced cancer immunotherapy. *Adv. Sci.* **2024**, *11*, 2307278.
[31] Bi, Y. Y.; Chen, Q.; Yang, M. Y.; Xing, L.; Jiang, H. L. Nanoparticles targeting mutant p53 overcome chemoresistance and tumor recurrence in non-small cell lung cancer. *Nat. Commun.* **2024**, *15*, 2759.
[32] Zawacka, J. E. p53 biology and reactivation for improved therapy in MDS and AML. *Biomark. Res.* **2024**, *12*, 34
[33] Yang, L. J.; Yao, C. C.; Su, Z. N.; Fang, Y. H.; Pandey, N. K.; Amador, E.; Diao, T.; Bao, G.; Cao, D. R.; Chen, X. H. et al. Combination of disulfiram and Copper-Cysteamine nanoparticles induces mitochondria damage and promotes apoptosis in endometrial cancer. *Bioact. Mater.* **2024**, *36*, 96–111.
[34] Mendoza, A.; Patel, P.; Robichaux, D.; Ramirez, D.; Karch, J. Inhibition of the mPTP and lipid peroxidation is additively protective against I/R injury. *Circ. Res.* **2024**, *134*, 1292–1305.